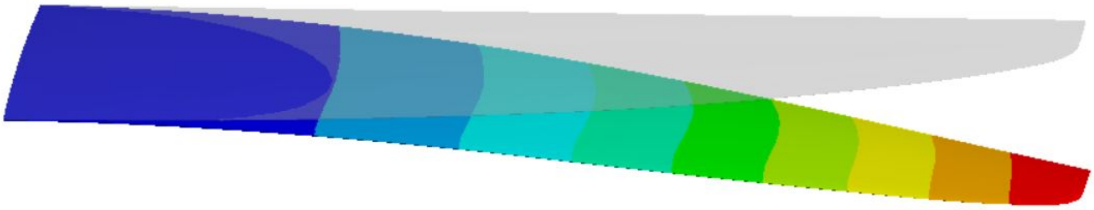

Hydrodynamic and Fluid-Structure Interaction analysis of a Windsurf Fin

André Roquette Quadros Saldanha

Thesis to obtain the Master of Science Degree in

Mechanical Engineering

Supervisors: José Manuel Da Silva Chaves Ribeiro Pereira
Leigh Stuart Sutherland

Examination Committee

Chairperson: Carlos Frederico Neves Bettencourt da Silva
Supervisor: Leigh Stuart Sutherland
Member of the Committee: Luís Rego da Cunha de Eça

October 2019

OUÇO E ESQUEÇO.
VEJO E LEMBRO.
FAÇO E COMPREENDO.

Acknowledgments

First and foremost, I would like to express my gratitude to both my advisors José Chaves Pereira and Leigh Sutherland for the given support during this project and for sharing their knowledge in their field of study. Thanks for having introduced me to the study of CFD and the structural study of composite materials, always with a practical approach to the study of hydrofoils. Thanks for the opportunity to work in this project that aroused an immense curiosity right from the beginning and for allowing me the freedom of exploring this subject in my own way.

I would like to acknowledge all the people responsible for the previous work done on this F-Hot Slalom Windsurf Fin and for making their work available which contributed a lot for the development of the present thesis. Thanks to the F-Hot Company for the opportunity to continue the investigation on their Fin and I hope they see my work as a relevant tool in the development of new Fins.

I would also like to thank all the professors and colleagues from IST and Tongji that taught me and influenced me a lot during these past years and were central in the process of acquiring the motivation, interest and technical competences needed to develop this project. A special props to Selvagens that have strongly accompanied me with resolute persistence over the last few years.

I'm extremely grateful to all my family and friends that throughout the years have believed in my potential and without whom this journey would have been much harder. A special thanks to Leonor that made this journey much easier and whose support I rely on for the future that awaits us. An extra-special emphasis to my parents that encouraged me and gave me the strength needed to overcome myself, helping and supporting me whenever needed over the past 24 years.

Resumo

Este trabalho consiste na criação de um modelo de Interação Fluido-Estrutura (FSI), com o objetivo de estudar as cargas hidrodinâmicas induzidas pela água numa quilha de Windsurf produzido pela F-Hot em materiais compósitos, bem como o estudo do seu comportamento mecânico quando em utilização. No decorrer do processo deste trabalho, foram realizados estudos estruturais e hidrodinâmicos da quilha de windsurf. Estes estudos são posteriormente acoplados com a finalidade de uma análise FSI. As condições analisadas para o estudo da quilha de Windsurf abrangem escoamentos com um número de Reynolds no intervalo de 3 x 10 ^{5} a 10 x 10 ^{5} assim como 3 diferentes ângulos de ataque. Estas condições representam as condições de navegação mais comuns em eventos de Slalom Windsurf. Quanto ao estudo do comportamento da quilha, três parâmetros diferentes são investigados: a força de sustentação da quilha, a deflexão máxima da quilha e o ângulo de torção na ponta da quilha. Para as simulações numéricas, foram utilizados dois softwares comerciais: ANSYS Workbench para a parte estrutural e Star CCM+ para a parte CFD do projeto. O processo aqui desenvolvido contribui para um melhor entendimento do comportamento estrutural da quilha, fornecendo resultados numéricos de maior precisão comparativamente a trabalhos anteriores.

Esta tese de mestrado é parte de uma investigação em curso de uma quilha de Windsurf, contando com a colaboração de diferentes instituições em Portugal e no Reino Unido.

Palavras-chave: Interação Fluido-Estrutura, Dinâmica dos Fluidos Computacional, Materiais Compósitos, Star CCM+, ANSYS, Quilha de Windsurf

Abstract

This work concerns the creation of a Fluid-Structure Interaction (FSI) model with the purpose of studying the water-induced hydrodynamic loads on the composite Windsurf Slalom Fin produced by F-Hot, as well as its structural behaviour when in operation. Along the process of this work, a structural and hydrodynamic studies of the Windsurf Fin are done. These studies are then coupled together with the finality of an FSI analysis. The analysed conditions for the study of the Windsurf Fin comprises flow conditions with a Reynolds number in the range of 3 x 10^5 to 10 x 10^5 as well as three different angles of attack. This range covers the various sailing conditions most probable in a Windsurf Slalom event. As for the study of the Fin's behaviour, three different parameters are investigated: the Fin's Lift Force, the maximum Fin's deflection and the twist angle at the Fin's tip. For the numerical simulations, two commercial software were used: ANSYS Workbench for the Structural part and Star CCM+ for the CFD part of the project.The process here developed contributes to a better understanding of the Fin's behaviour, providing better and more accurate numerical results compared to previous works.

This MSc thesis is part of an ongoing investigation of a Slalom Windsurf Fin relying on the collaboration between different institutions in Portugal and the United Kingdom.

Keywords: Fluid-Structure Interaction, Computational Fluid Dynamics, Composite Material, Star CCM+, ANSYS, Windsurf Fin

Contents

List of Tables

List of Figures

Nomenclature

Abbreviations

3D	Three-Dimensional
ACP	ANSYS Composite PrepPost
AoA	Angle of Attack
APDL	ANSYS Parametric Design Language
CAD	Computer-Aided Design
CFD	Computational Fluid Dynamics
FEM	Finite Element Model
FRC	Fiber Reinforced Composite
FSI	Fluid-Structure Interaction
FVM	Finite Volume Method
GRP	Glass Reinforced Plastic
IST	Instituto Superior Técnico
LASEF	Laboratory of Fluid Simulation in Energy and Fluids
LSB	Laminar Separation Bubble
NSE	Navier-Stokes Equations
PAC	Passive Adaptive Composite
PL	Prism Layer
RANS	Reynolds Average Navier-Stokes
RF	Relaxation Factor
TM	Turbulence Model
VOR	Volume of Refinement

Boundary Layer Parameters

δ	Boundary Layer thickness
τ_w	Wall Shear Stress
u_τ	Friction Velocity
u^+	Dimensionless velocity
y^+	Dimensionless wall distance

Fluid and Structure Properties

μ	Dynamic Viscosity
ν	Kinematic Viscosity
ρ	Density
E	Young's Modulus
g	Gravitational acceleration
p	Absolute Pressure
V, U_∞, v	Fluid's velocity

Geometry Parameters

Æ	Aspect Ratio
Λ	Sweep Angle
λ	Taper Ratio
b	Wing Span
c	Chord length
c_r	Chord length at the Roof of the Fin
c_t	Chord length at the Tip of the Fin
S, A	Fin's Surface Area

Hydrodynamic Parameters

α	Angle of Attack
α_i	Induced Angle of Attack
α_{eff}	Effective Angle of Attack
v_i	Induced Velocity

a_{2D}, a_{3D}	Lift Coefficient derivative in relation to the AoA for 2D and 3D
C_d, C_D	Drag Coefficient
C_f	Skin Friction Coefficient
C_l, C_L	Lift Coefficient
C_p	Pressure Coefficient
D	Drag Force
L	Lift Force
Re	Reynolds Number

Grid Convergence Parameters

δ_{RE}	Error Estimation
ϕ_0	Estimated Exact Solution
ϕ_i	Numerical Solution of grid i
h_i	Number of cells in grid i
r_i	Mesh Characteristic Number
U	Numerical Uncertainty

Turbulent Flow Parameters

ϵ	Dissipation of Turbulent Kinetic Energy
γ	Intermittency Factor
ω	Specific Rate of dissipation of Turbulent Kinetic Energy
τ_{ij}	Turbulent Stress Tensor
$\widetilde{\nu}$	Turbulence Viscosity
k	Turbulent Kinetic Energy

Chapter 1

Introduction

The sport of Windsurf as we know it today has been around since the 1960's and it was created based on the simple idea of a board equipped with as sail and moved by the force of the wind.
The beginning of the conceptualization of the sport was responsibility of Newman Darby. Sailboats were already in use for centuries, and Darby with the idea of simplifying and doing an adaptation of a sailboat, in 1948 assembled a hand-held sail to a universal joint fixed to a floating board calling it sailboarding. The Sailboard is nowadays known as Windsurf.
This simple invention spread all over the world and has gained a lot of supporters. With the rising popularity, the whole design and concept of windsurfing has been, year after year, improved and changed to adapt to each type of riding and each type of rider.
Nowadays windsurfing is used mainly for leisure and competitive purposes with the competitive aspect growing a lot in recent years, being one of the sailing events on the Olympic Games in Tokyo 2020, the RS:X [1]. This increase of competitiveness has been observed by designers and manufacturers of windsurf equipment, and hence big efforts have been made to design and create the best windsurf gear to suit the requirements of each rider.

1.1 Motivation

The aspiration for a better design of a Windsurf Fin is the main purpose of this study.
The improvement of technology, the availability of Engineering software that allows a precise analysis of the equipment and accessibility of new materials better suited for the production of windsurf equipment has been important factors for the rapid evolution and constant change of the sport's concept. Different riders and different conditions require different equipment, and nowadays this constant control over the type of gear used is an important differentiation factor when in a competition. With everyday newly available technologies, this kind of studies has become much more doable and efficient.
The task of producing a high loaded structure, able to resist to such loads and to behave in a specific and pre-established way, is nowadays possible due to composite materials as well as its production, namely the layers' orientation and composition.

Besides the great advances that have been made with the composites usage in the aeronautical world, an equally important technological improvement has occurs, the availability of software able to virtually predict the behaviour of certain structures in an efficient way at low costs, without the need for expensive and time-consuming tests of physical models. These technologies include Finite Element Models (FEM) analysis to study the structural behaviour of complex and, in this case, anisotropic structures. Also, the use of Computational Fluid Dynamics (CFD), that allows a trustworthy analysis of the fluid around the structure, as well as the ability to calculate the load exerted on the structure by the moving fluid. All these numerical analyses allow a more reliable, cheap and efficient way of testing structures before their production.

1.2 Objectives

The objective of this work is a combination of several studies: to make a Hydrodynamic study of a Windsurf Fin through a CFD analysis, and also a Structural FE analysis of the same Fin. Subsequently, a joint analysis of both Hydrodynamic and Structural studies will culminate in a Fluid-Structure Interaction (FSI) analysis, this is the final purpose of the present work, to develop a model capable of doing an FSI analysis and to provide results and technologies for eventual future works. The Fin to be analysed is a composite Slalom Fin made by F-Hot Company and design by Steve Cook.

All these simulations will be done with the main purpose of having an overall understanding of the Fin in regards to its operation load and behaviour when loaded.

This work is a piece in the line of previous studies, with the focus to analyse the behaviour of a Windsurf Fin and provide data and the technologies for a future work where ultimately a Passive Adaptive Composite (PAC) analysis is done, tailoring the response of the structure by changing the orientation of the composite plies [2]. This is the main objective of all the past, present and future work related to this Fin, to be able to create the technology capable of building a structure that behaves exactly as desired.

1.3 State of the Art

1.3.1 Composites and CFD analysis in boat design

The latest developments in terms of composite materials and the ability of numerically testing its capabilities, have been present in modern maritime sports design.

Before, the composites used in maritime construction were much less reliable, being much more prone to break when charged with high loads. The fiberglass or GRP is a perfect example of these composites that were (and still are) commonly used in naval construction.

Materials science and composite technology are progressing, and new types of composites include carbon nanotubes and epoxy blends. The carbon composites materials were earlier reserved for small crafts and high-tech components. Nowadays, these types of materials have been popularized by naval constructors. This is mostly due to the crescent ease of producing them and the growing of engineering challenges such as new ways of sailing, for example, the appearance of horizontal hydrofoils that create vertical lift allowing sailing boats and board to fly. The cost of carbon fiber is high compared to other composites, but it will naturally fall as the volume of production increases. Lightness, strength, durability and a growing ease of production are characteristics of carbon composites materials, this means that naturally, these materials will be more and more in use not only for naval purposes but also for Aerospace, Automotive, Civil and many other industries.

The use of composite materials for flying maritime yachts have been pushed to the highest level of detail and scientific demand. A good example of these efforts is the latest editions of the America's Cup, which have been more and more demanding in terms of scientific research related to the design of the hydrofoils as well as the composite laminate that is highly loaded and have to sustain a huge amount of oscillating loads. For these necessary studies of the foils and the composite materials, similar analysis to the ones in the present work (CFD and FSI analysis) are done to test the boat components before producing them.

Figure 1.1: AC75 - 36th America's Cup boat [3]

1.3.2 Windsurf and types of fins

In the world of windsurfing, the use of composite Fins has been widely used by windsurfers. The equipment has evolved through a process of trial and error, based on the windsurfer's feeling of the board, sail and fin. Contrarily to the board and sail, the Fin is not so easy to improve due to the fact that it is submerged, and the windsurfer does not have such a good understanding of its behaviour when in use. With the growing of the sport, people have paid more attention to the role of the fin, and since then, have done big efforts to improve its performance.

The choice for carbon made Fins is justified by its better performance. Despite the higher price tag, carbon delivers a more reliable lift and allows the creation of stiff and low twist fins often preferred by racers.

Regarding the types of Fins in the market today, there is a big variety. Different Fins are used for different purposes. Among the most used Fins, there are: Race Fins, Free-ride Fins, wave fins and Slalom Fins. Each of the previously mentioned Fins has different characteristics that allow a better performance for its specific use. Different length, width, profile, material and arrangement of composite layers, allow the rider different performances, having influence on the board's grip, directional stability, carving ability...

Figure 1.2: Wave Fin (left) and Race Fin (right)

The Fin that will be studied in the present work is a slalom Fin produced by F-Hot [4]. The slalom Fins are usually long and slender, provide a good ratio of lift to drag and are very versatile which allow the rider to sail in different conditions and speeds and avoids the foil to stall due to flow separation.

Figure 1.3: F-Hot Slalom Fin 37cm

1.4 Contributions

Few recent works have focused on this topic. Despite the increasing popularity, the fact that windsurf is mainly used for recreation purposes, scientific and more detailed approaches to the subject of design and production of windsurf components have not been a priority. But the fact that nowadays the tools for a more detailed analysis of the subject have become widely available and easily employed, have given way to the interest of many producers that wish meticulously tuned gear able to respond as intended.

This work arises with the intention of complementing a sequence of several other recent studies that have been developed in IST concerning the analysis of a Windsurf Fin.

The topic was addressed in 1993 by Sutherland [5], and since then the author has manifested the interest of further investigating the subject, ultimately getting to a rigorous and close to reality analysis of the behaviour of the Windsurf Fin when in operation.

Related works have been made more recently by Nascimento [6], who focused on the study of the structural simulation of this Windsurf Fin through Finite Element Model analyses. This study was then further explored by Balzer [7]. Both the previously named author focused solely on the structural aspect of the analysis of this Fin. Regarding the hydrodynamic aspect of the project, a study by Santos [8] that focused on the analysis of the fluid flow around the same Windsurf Fin, gives attention to the obtainment of the hydrodynamic loads on the Fin.

All these studies done have proven to be significant steps towards a final and meticulous study of the Windsurf Fin. The present thesis will contribute as one of the final steps of this continuous work that has been developed for the past several years, being the major objective to compile the structural and hydrodynamic analysis through a process of Fluid-Structure Interaction.

1.5 Thesis Outline

Regarding the structure of the present work, it comprises 7 main chapters.

The first Chapter presents an introduction to the work done, with a brief explanation of the main purposes of it, providing a clarification for the topic's choice and its interest to the scientific community as well as to the Windsurf panorama.

The second Chapter will introduce some basic Aero-Hydrodynamic concepts of sailing as well as structural composites concepts that will enable a better understanding of later results. Also, in this section, an explanation to the Fin's role when sailing and a brief physical clarification will be presented.

The third Chapter covers the Hydrodynamic study, starting with a process of verification and validation of the turbulence model used as well as the discretization model. In this Chapter, it's presented the Hydrodynamic model used, including all the selected parameters used for the CFD analysis. It's also shown, a look over the CFD process and the steps done for each simulation.

The fourth Chapter will be about the Structural analysis of the Windsurf Fin. It will clarify the composite laminate layup and present the structural Finite Element Model (FEM) used for the future Fluid-Structure Interaction (FSI) Analysis. This Chapter starts with a description of the calibration done to the Structural model and follows with a presentation of the steps taken during the structural simulations process.

The fifth Chapter presents the procedures for the Fluid-Structure Interaction (FSI) analysis. It talks about the restrictions and limitations associated with the process, the issues faced during its development and how these issues were overcome. It clearly presents the FSI analysis model and steps taken along the process. It also shows 2 concrete cases of this FSI analysis and how the results change along the various iterations.

Chapter six, presents the FSI results for 3 established parameters. Some conclusions and assessments are done to the mechanical behaviour of the Fin with the focus on getting to know how the structure reacts to the hydrodynamic loads and its effects on the overall performance of the sailing Windsurf.

Chapter seven, serves as a conclusion to the FSI study of the Windsurf Fin, exposing the major achievements of this project and refers to possible future work to be done to proceed with this Fin's study, with the main objective of creating the technology capable of building a tailor-made structure that behaves exactly as wanted.

Chapter 2

Theoretical Background

2.1 Aero-Hydrodynamic Concepts

2.1.1 Aerofoil

The Aerofoil is a curved profile geometry that creates forces perpendicular to the incoming flow, lift force, much higher than the forces parallel to this incoming flow, drag force. It is the cross-sectional shape of a wing, blade, sail, Fin and many other structures intended to generate these aerodynamic forces. In the specific case of the Fin studied in the present work, it is a structure to be operated with water as working fluid, therefore, it is called hydrofoil.

Terminology speaking, there are some basic concepts of a foil to have in mind when analysing it. These concepts are related to its geometry. The leading edge, which is a rounded edged and the foremost edge of an aerofoil section; the trailing edge is the sharp edge located at the rear section of the aerofoil section; the chord, which is the straight line that connects the leading and trailing edge; and the camber line which is the line that connects the leading and trailing edge of the aerofoil, being equidistant from its upper and lower surfaces.

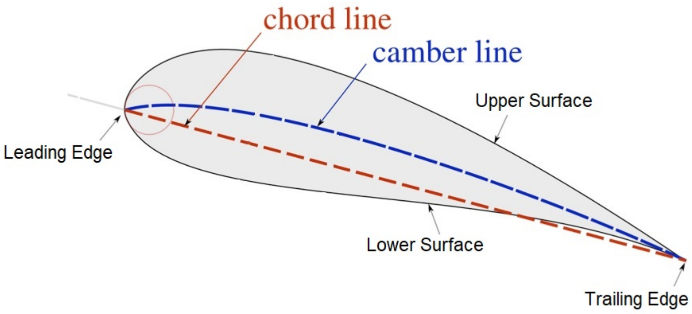

Figure 2.1: Aerofoil Nomenclature

When the chord and the camber line are coincident, then it is a symmetric foil, as it is the Windsurf Fin hydrofoil here analysed.

When a hydrofoil is moving through fluid, it generates hydrodynamic forces. These forces can be de-composed into two components. The Lift force, which is perpendicular to the incoming flow, and the Drag force, that is parallel to the incoming flow.

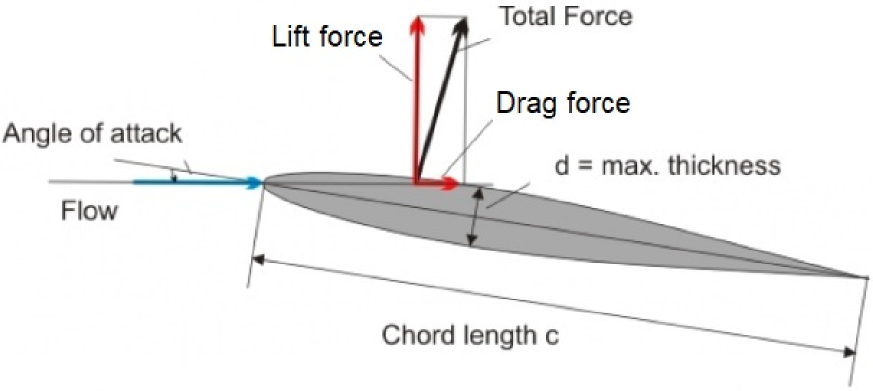

Figure 2.2: Aerodynamic Forces on Foil

The shape of the foil, its angle of attack (angle between the incoming flow and the chord line) and the properties of the incoming fluid flow, are the main parameters on which the hydrodynamic forces depend on. For most cases, the perfect configuration of profile and angle of attack is the one that increases to a maximum the lift to drag ratio.

In order to be able to quantify the lift force, the drag force and the pressure distribution on a foil and to compare them between different foils with different profile geometries, the dimensionless numbers can be employed. For that, the lift, drag and pressure coefficients are usually used. These coefficients are defined as follows for 3D wings.

$$C_L = \frac{L}{\frac{1}{2}\rho V^2 S} \tag{2.1a}$$

$$C_D = \frac{D}{\frac{1}{2}\rho V^2 S} \tag{2.1b}$$

$$Cp = \frac{p - p_\infty}{\frac{1}{2}\rho_\infty V_\infty^2} \tag{2.1c}$$

Both the lift and the drag are highly dependent on the angle of attack. The lift force is regarded as having a linear variation with the varying angle of attack for small angles of attack (Figure 2.3). With the increasing AoA, after a critical point, the flow around the foil will separate, losing its lift. This phenomenon is called stall.

The graph from Figure 2.3 shows the variation of the Lift Coefficient with the AoA. It is clear that this specific foil is a symmetric foil due to its zero lift for zero AoA. The critical point of stall can be observed at an AoA of 15 degrees, this AoA is called the critical angle of attack. For AoA bigger than 15 degrees, the flow around the foil separates and foil stalls, loosing abruptly its lift. The following images show the

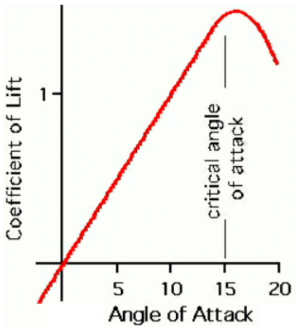

Figure 2.3: Lift Coefficient vs. Angle of Attack of a generic symmetric foil

moment of stall of an asymmetric aerofoil.

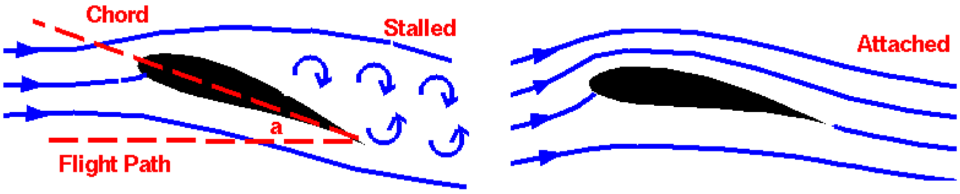

Figure 2.4: Representation of a stalled foil (left), and an attached flow around a foil (right)

2.1.2 Finite wings

For the case of three-dimensional wings, or finite wings, there are some other geometrical considerations to have in mind when evaluating it.

The Span (b) is the distance between both wingtips. For the particular case of the Windsurf Fin, the Span is considered to be the distance between the root and the Fin tip. The chord might not be constant along the span, so the chord variation along the span must be quantified. Two important chord lengths are the root chord (r_C) and the Tip Chord (t_C), which are the chord at the root and tip of the Fin, respectively. The Sweep angle (Λ) is generally described as the angle between the leading edge and the line perpendicular to the root profile. Figure 2.5 shows the above-mentioned parameters.

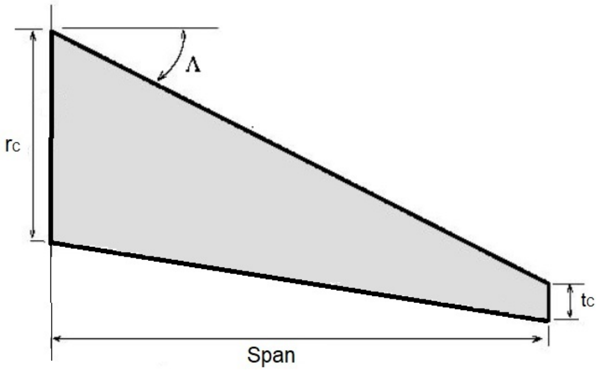

Figure 2.5: Finite wing geometrical parameters

Another geometrical features of the Finite wing are the Taper Ratio (λ) and the Aspect Ratio (Æ). The λ is the ratio between the chord length at the tip and at the root of the wing [$\lambda = \frac{C_t}{C_r}$]. The Æ is the ratio between the squared of the wingspan (b) and the wing area (S) [Æ $= \frac{b^2}{S}$].

In the Finite wings, we can observe the phenomenon of longitudinal vorticity that occurs along its entire span with higher intensity in the wingtip region. This phenomenon is caused by the differential of pressure between the upper and lower surface of the wing, responsible for the lift, and the tendency of these pressure differences to cancel each other out in the marginal edges (Tip region). Transversal velocity components are created in this region that lead to the displacement of the flow current lines generating vorticity. Generally, in an airplane wing with upward lift, the flow current lines in the upper surface are displaced inward as schematically represented in Figure 2.6 (a). Figure 2.6 (b) presents a simulation on Star CCM+ of the Tip Vortex on the Windsurf Fin used for this work. In this representation, a velocity of 10 Knots (5.144 m/s) and an Angle of Attack of 10 degrees was chosen.

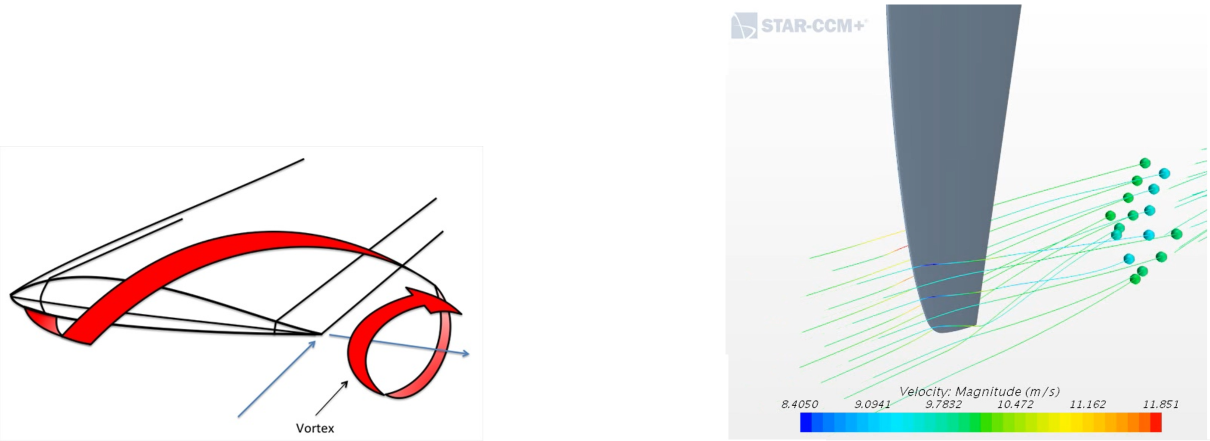

(a) Schematic View

(b) CFD Simulation View

Figure 2.6: Tip Vortex

This longitudinal vorticity is responsible for the appearance of a field of descending induced velocities (v_i), so, each wing section will now be working with a different effective velocity field which will result in the variation of the angle of attack by a quantity of

$$\alpha_i = tan^{-1}\left(\frac{v_i}{U_\infty}\right) \approx \frac{v_i}{U_\infty} < 0 \tag{2.2}$$

This quantity is designated as the induced angle of attack. Each wing section installed at a geometric angle of attack α in relation to the incoming flow U_∞, responds now as operating at an effective angle of attack $\alpha_{eff} = \alpha + \alpha_i < \alpha$. Figure 2.7 clearly shows these different angles of attack in a section of a Finite wing.

The appearance of this vortex disturbed flow will have some consequences in terms of Lift and Drag. This Vorticity will create an induced drag [$D_i = Lsin(\alpha_i) \approx L\alpha_i$], therefore increases the overall wing drag, and also will decrease the effective angle of attack, decreasing the effective Lift on the wing. The overall effect of this longitudinal vortex is bad for the aerodynamic performance of the wing, that is why in some airplanes, some vertical wingtips (winglets) have been implemented to diminish the impact of

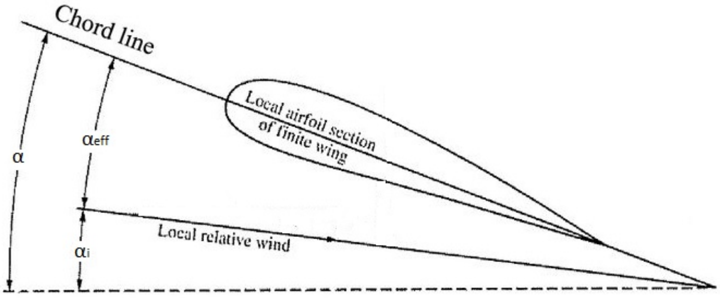

Figure 2.7: Geometrical, Induced and Effective Angle of Attack

the tip vortex and to try not to compromise the aerodynamic performance. An observation that can be made regarding the lift coefficient for 3D wings, is that its derivative in relation to the AoA, $\frac{\partial C_L}{\partial \alpha}$, for infinite wings is bigger than that for Finite wings. This can be observed in the following Figure 2.8.

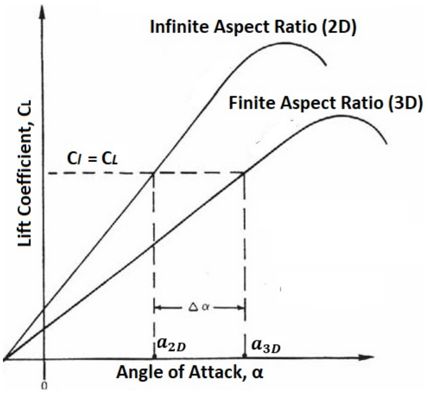

Figure 2.8: C_L vs. α for 2D and 3D wings

The lift coefficients derivative in relation to the angle of attack for 2D and 3D is represented by:

$$a_{2D} = \left(\frac{dC_L}{d\alpha} \right)_{2D} \tag{2.3a}$$

$$a_{3D} = \left(\frac{dC_L}{d\alpha} \right)_{3D} \tag{2.3b}$$

So, based on Figure 2.8 and equations 2.3a and 2.3b, it can be stated that $a_{2D} > a_{3D}$.
A correlation involving the growth rate of the lift coefficient with the increasing AoA for 2D and 3D wings can be established. Based on the Prandtl lifting line theory, for rectangular wings and potential flow (inviscid, incompressible and irrotational flow), the correlation between a_{2D} and a_{3D} is only dependent of the aspect ratio (Æ) [9].

$$a_{3D} = \frac{a_{2D}}{1 + \frac{a_{2D}}{\pi \text{Æ}}} \tag{2.4}$$

2.1.3 Laminar - Turbulent Boundary Layer Flow

As a body moves through a fluid or a fluid passes over a body, the fluid velocity profile near the surface is disturbed. As the fluid passes through the object, the viscous flow sticks to the wall, and the molecules just above the surface are slowed down, these molecules, in turn, slow down the flow just above them. This creates a thin layer of flow near the wall, with a varying velocity profile, called boundary layer.

The boundary layer in fluid mechanics is the near-wall region where the effects of viscosity are significant and the velocity profile of the flow varies from the wall velocity (at the wall) up until the free stream velocity (at the end of the boundary layer). The principal reason for the existence of a boundary layer is due to the viscous properties of the fluid flow and the no-slip boundary condition at the surface.

The boundary layer can be either laminar or turbulent depending on the value of the Reynolds number. A laminar boundary layer is a smooth with well-defined velocity profile layer, while the turbulent boundary layer is dominated by flow swirls or eddies, its velocity profile is much harder to define and it is responsible for the appearance of a bigger skin friction drag. The velocity profile of a laminar boundary layer over a semi-infinite flat plate is shown in Figure 2.9. In this figure, u_0 is the free stream flow velocity, $u(y)$ is the variation of the velocity along the perpendicular direction of the plate and δ is the thickness of the boundary layer at a certain point of the plate.

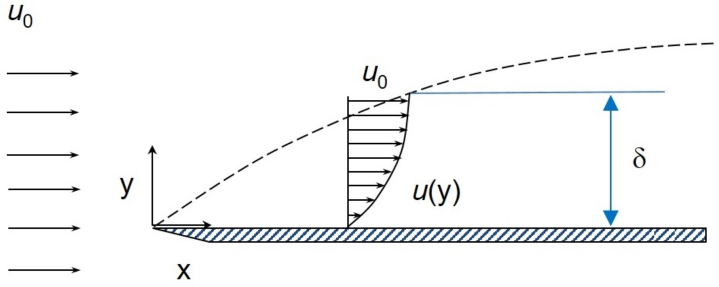

Figure 2.9: Laminar Boundary Layer over flat plate

A Turbulent boundary layer is a more complex flow, the fluctuations of the velocities are random, so the analytic analysis of this flow must be done through statistical methods instead of deterministic ones, so, rises the necessity of quantifying the flow using parameters such as the mean velocity values (u) and the intensity of the fluctuations around the mean value (u'). As shown in Figure 2.10, the turbulent flow is composed by the overlapping of the mean velocity with the fluctuations of this parameter $\tilde{u} = u + u'$.

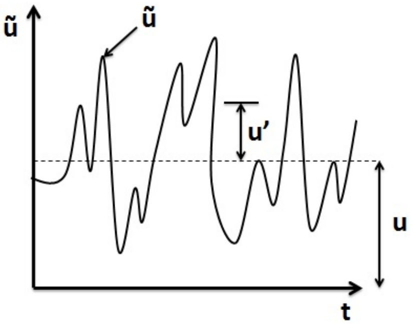

Figure 2.10: Turbulent Fluctuations around a constant mean velocity value

Some adimensional parameters are used to characterize the turbulent flow in a boundary layer, such as the dimensionless wall distance y^+ and the dimensionless velocity u^+. Both parameters are defined as follows in equation 2.5:

$$y^+ = \frac{yu_\tau}{\nu} \qquad u^+ = \frac{u}{u_\tau} \tag{2.5}$$

Being y the absolute distance from the wall, ν the kinematic viscosity , u the mean velocity and u_τ the friction velocity defined as:

$$u_\tau = \sqrt{\frac{\tau_w}{\rho}} \tag{2.6}$$

Where τ_w is the wall shear stress which is dependent on the skin friction coefficient (C_f) which can be empirically defined as a function of the Reynolds number.

$$C_f = 0.026Re^{-1/7} \tag{2.7a}$$

$$\tau_w = \frac{C_f \rho U_\infty^2}{2} \tag{2.7b}$$

The turbulent boundary layer can be divided into two sections, the inner layer and the outer layer. Figure 2.11 shows the dimensionless velocity profile (u^+) along the dimensionless wall distance (y^+).

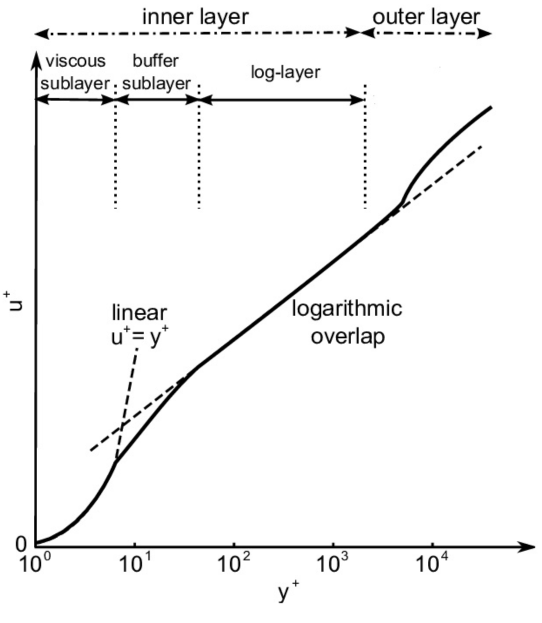

Figure 2.11: u^+ vs. y^+ in a Turbulent boundary layer in semi-logarithmic coordinates

The inner layer goes from the wall until around 15% of the boundary layer thickness, the outer layer comprises the rest of the boundary layer. The inner layer can yet be subdivided into three sections:

- The viscous sublayer ($y^+ < 5$), is dominated by the viscous effects and has a linear behaviour defined by $u^+ = y^+$

- The logarithmic layer ($y^+ > 30 - 50$) where the turbulence stress dominates the flow. The velocity profile function is given by $u^+ = \frac{1}{k}ln(y^+) + B$ where k is the Karman constant (k=0.41) and B=0.51 is a constant.

- The buffer sublayer ($5 < y^+ < 30 - 50$), is the transition part of the flow between the viscous-dominated region and the turbulence-dominated region

A very important concept in boundary layer theory is the moment of transition from laminar to turbulent. As previously mentioned, the type of boundary layer, laminar or turbulent, depend upon a dimensionless parameter called the Reynolds number given by [$Re = \frac{\rho vc}{\mu}$], where ρ is the fluid density, u the velocity of the fluid with respect to the object, c the characteristic linear dimension and μ the dynamic viscosity. This number represents the ratio of inertial forces to viscous forces within a fluid which is subjected to relative internal movement.

Depending on the magnitude of the Reynolds number, apart from other factors, the flow can be laminar, turbulent or it can be in a critical state where the flow is transitioning from laminar to turbulent, in this case, the Reynolds number is said to be critical.

Analysing the critical Reynolds Number is an extraordinarily complicated process and it is quantified for only a few specific geometries. For the case of a boundary layer flow over a flat plate, which can then be extrapolated for a low curvature wing surface, the critical Reynolds number is around 500,000, but it can vary depending on surface roughness and other factors. A representation of the transition of a boundary layer over a flat plate from laminar to turbulent is pictured in Figure 2.12. It is possible to clearly see the transition region of the flow as well as the different subdivisions of the turbulent boundary layer.

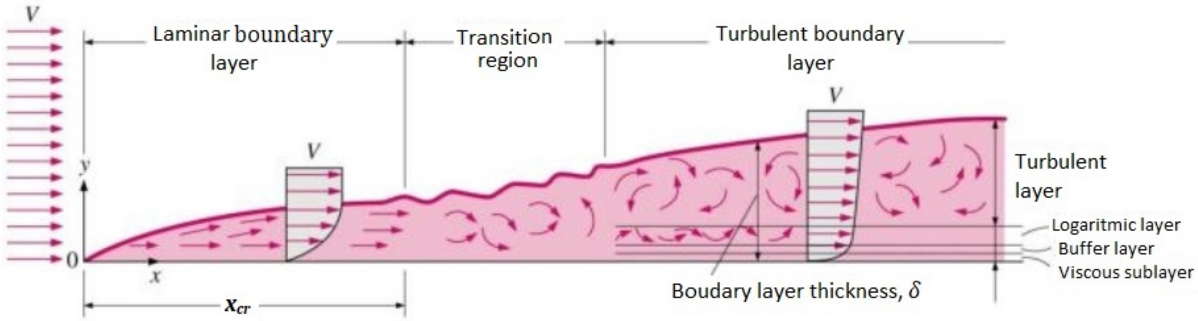

Figure 2.12: Velocity profile of a turbulent boundary layer

The turbulent boundary layer has an increased shear stress at the body surface when compared with flow in a laminar boundary layer. This increase of the shear stress at the wall increases the friction drag and at the same time, makes the flow less susceptible to flow separation when faced with adverse pressure gradient.

So, in the case of a flow over a wing, it is sometimes advantageous to have a turbulent flow for the simple fact that the turbulent boundary layer tends to sustain an adverse pressure gradient better than a laminar boundary layer and so, it separates with greater difficulty, which is good to avoid the wings stalling.

The pressure gradient along the surface is also a factor that affects the boundary layer. The pressure gradient along the flow direction $\left[\frac{dp}{dx}\right]$ can be zero, positive (adverse) or negative (favorable).
When the pressure gradient is adverse $\left[\frac{dp}{dx} > 0\right]$, it means that the pressure increases in the direction of the flow and therefore, the flow velocity decreases. If the adverse pressure gradient is sufficiently strong, the flow velocity inside the boundary layer will fall to zero, at this point, the fluid flow becomes detached from the surface and the portion of the boundary layer closest to the wall reverses in flow direction. A representation of this situation is represented in Figure 2.13.

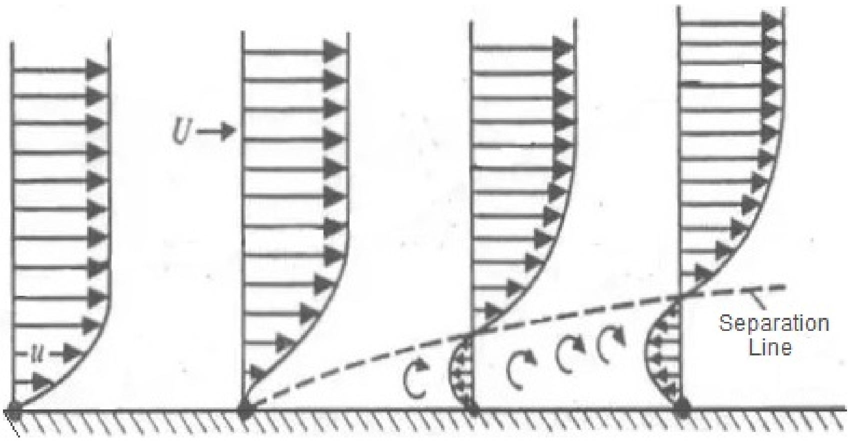

Figure 2.13: Schematic view of the separation of a boundary layer with an adverse pressure gradient

In the case of favorable pressure gradient $\left[\frac{dp}{dx} < 0\right]$, the pressure decreases in the direction of the flow, so, the velocity inside the boundary layer will increase. If large enough, this favorable pressure gradient in a turbulent boundary layer, can cause a return to laminar flow [10].

2.2 CFD analysis and Navier-Stokes

Computational Fluid Dynamics (CFD) is extensively used for studies of fluid flow, being a great benefit of using it the fact that experimentally testing fluid flow conditions is often prohibitively expensive and time-consuming.
Analytical solutions for these types of complex problems do not exist, only for very few and simple cases, therefore, new methods were needed in order to numerically solve these more complex problems.
It is important to be acquainted with some disciplines to be able to perform good CFD calculation and to obtain reasonable results:

- Fluid Mechanics
- Mathematics
- Computer science
- Geometry modeling and meshing

Assuming incompressible and steady flow, the governing equations for fluid flow are the Navier-Stokes Equations (NSE) written in a vector form as follows in Equation 2.8. Four partially differential equations that represent mass conservation (continuity equation), and the momentum conservation equation (one for each coordinate i, j, k) for an infinitesimal fluid element.

$$\nabla.\vec{V} = 0 \tag{2.8a}$$

$$\frac{D\vec{V}}{Dt} = -\frac{1}{\rho}\nabla p + \nu\nabla^2\vec{V} + \vec{g} \tag{2.8b}$$

Where $\frac{Du}{Dt}$ is the material derivative defined as $\frac{\partial}{\partial t} + u.\nabla$. These equation systems can then be rewritten in a derivative form for steady incompressible flow as follows in Equation 2.9.

$$\frac{\partial u_i}{\partial x_i} = 0 \tag{2.9a}$$

$$u_j\frac{\partial u_i}{\partial x_j} = -\frac{1}{\rho}\frac{\partial p}{\partial x_i} + \nu\frac{\partial^2 u_i}{\partial x_j x_j} + f_i \tag{2.9b}$$

Taking into consideration that not every flow condition can be simplified as an incompressible, steady and laminar flow, to be able to calculate and characterize turbulent flow, considering their random fluctuations around a mean value, a statistical approach to the NSE is conducted.
Using a time-averaging method known as Reynolds averaging of the fluctuations to the continuity and momentum equations, these equations are then solved for their mean value leading to the appearance of the Reynolds Average Navier Stokes (RANS) equations.

$$\frac{\partial \overline{u_i}}{\partial x_i} = 0 \tag{2.10a}$$

$$\overline{u_j}\frac{\partial \overline{u_i}}{\partial x_j} = -\frac{1}{\rho}\frac{\partial \overline{p}}{\partial x_i} + \nu\frac{\partial^2 \overline{u_i}}{\partial x_j x_j} + \frac{1}{\rho}\frac{\partial}{\partial x_j}(-\rho\overline{u_i'u_j'}) \tag{2.10b}$$

Where $-\rho\overline{u_i'u_j'}$ can be defined as the turbulence stress tensor τ_{ij}, also known as the Reynolds stress tensor. For a more generic description of the RANS equations, the previous equations 2.9 can be written for the three spatial coordinates x, y and z, and for a case of steady incompressible flow.

$$\frac{\partial u}{\partial x} + \frac{\partial v}{\partial y} + \frac{\partial w}{\partial z} = 0 \tag{2.11a}$$

$$u\frac{\partial u}{\partial x} + v\frac{\partial u}{\partial y} + w\frac{\partial u}{\partial z} = -\frac{1}{\rho}\frac{\partial p}{\partial x} + \frac{1}{\rho}.\left(\frac{\partial \tau_{xx}}{\partial x} + \frac{\partial \tau_{xy}}{\partial y} + \frac{\partial \tau_{xz}}{\partial z}\right) \tag{2.11b}$$

$$u\frac{\partial v}{\partial x} + v\frac{\partial v}{\partial y} + w\frac{\partial v}{\partial z} = -\frac{1}{\rho}\frac{\partial p}{\partial y} + \frac{1}{\rho}.\left(\frac{\partial \tau_{yx}}{\partial x} + \frac{\partial \tau_{yy}}{\partial y} + \frac{\partial \tau_{yz}}{\partial z}\right) \tag{2.11c}$$

$$u\frac{\partial w}{\partial x} + v\frac{\partial w}{\partial y} + w\frac{\partial w}{\partial z} = -\frac{1}{\rho}\frac{\partial p}{\partial z} + \frac{1}{\rho}.\left(\frac{\partial \tau_{zx}}{\partial x} + \frac{\partial \tau_{zy}}{\partial y} + \frac{\partial \tau_{zz}}{\partial z}\right) \tag{2.11d}$$

Being τ_{ij} the Reynolds stress tensor defined as follows in equation 2.12

$$\tau_{ij} = \mu \left(\frac{\partial u_i}{\partial x_j} + \frac{\partial u_j}{\partial x_i} \right) - \rho \overline{u_i u_j} \tag{2.12}$$

Where the first equation is the Continuity equation for mass conservation and the three other equations are the conservation of momentum equation for x, y and z respectively.
When computing turbulent flow, the RANS equations are widely used, however, the system of equations 2.11 is not closed, so, additional equations are needed to calculate the turbulence Reynolds tensor τ_{ij}, hence the need for turbulence models to close the equation systems.
These turbulence factors can be calculated via the turbulent kinetic energy that can be written as $\overline{k} = \frac{1}{2}\overline{u_j'^2}$

There are several turbulence models with different specifications that can be used and are already implemented in commercial codes. From those, the ones that will be debated in the present work are:

- $k - \epsilon$, Standard Turbulence model
- $k - \omega$ SST Turbulence model
- $k - \omega$, $\gamma - Re_\theta$ Turbulence model
- Spalart-Allmaras Standard Turbulence Model

2.2.1 $k - \epsilon$ Standard Turbulence model

The k-epsilon is one of the most common turbulence models used. It is a two-equation model. These partial differential equations solve the turbulence of the flow for two distinct transported variables, the turbulent kinetic energy (k) and the dissipation of turbulence energy (ϵ).
This model is widely used for industrial and scientific purposes and gives good results for flows with relatively small pressure gradients and also for free-shear layer or mixing layer flows. Its accuracy has been experimentally shown to be reduced for adverse pressure gradients [11]
The Transport equations that compose this turbulence model are given by Equation 2.13

$$u\frac{\partial k}{\partial x} + v\frac{\partial k}{\partial y} = \nu_t S^2 + \nabla . \left(\left(\nu + \frac{\nu_t}{\sigma_k} \right) \nabla k \right) - \epsilon \tag{2.13a}$$

$$u\frac{\partial \epsilon}{\partial x} + v\frac{\partial \epsilon}{\partial y} = C_1 \frac{\epsilon}{k} \nu_t S^2 + \nabla \left(\left(\nu + \frac{\nu_t}{\sigma_\epsilon} \right) \nabla \epsilon \right) - C_2 \frac{\epsilon^2}{k} \tag{2.13b}$$

Here, ν_t is the modelling turbulent viscosity $\left[\nu_t = C_\mu \frac{k^2}{\epsilon}\right]$ and C_μ, C_1, C_2, σ_k and σ_ϵ are model constants. Refer to Appendix A.1 for detailed model equations

2.2.2 $k-\omega$ SST Turbulence model

The $k-\omega$ SST model was developed by Menter [12] and is the combination of the classic $k-\omega$ model developed by Wilcox and the well-known $k-\epsilon$ model.

The $k-\omega$ turbulence model is a two-equation system intended to predict turbulence by its partial differential equations for two variables, the turbulent kinetic energy (k) and the specific rate of dissipation of this turbulent kinetic energy (ω). The Shear Stress Transport (SST) formulation is an improvement done to the classical model that enhances the equation's behaviour both in the near-wall and in the far-field regions.

The $k-\omega$ SST model is known for being a very versatile model and generally having a good behaviour in adverse pressure gradient and flow separation. It is defined by the following two equations:

$$U_j \frac{\partial k}{\partial x_j} = P_k - \beta^* k\omega + \frac{\partial}{\partial x_j}\left[(\nu + \sigma_k \nu_T)\frac{\partial k}{\partial x_j}\right] \tag{2.14a}$$

$$U_j \frac{\partial \omega}{\partial x_j} = \alpha S^2 - \beta\omega^2 + \frac{\partial}{\partial x_j}\left[(\nu + \sigma_\omega \nu_T)\frac{\partial \omega}{\partial x_j}\right] + 2(1-F_1)\sigma_{\omega^2}\frac{1}{\omega}\frac{\partial k}{\partial x_i}\frac{\partial \omega}{\partial x_i} \tag{2.14b}$$

Where ν_T is the kinematic eddy viscosity. F_1, F_2 and P_k are auxiliary relations dependent on the turbulent kinetic energy (k) and on the specific dissipation rate (ω). All the other variables are closed coefficients, constants and some dependent on each other [13] . Refer to Appendix A.2 for detailed equations

2.2.3 $k-\omega$, $\gamma - Re_\theta$ Turbulence model

The $\gamma - Re_\theta$ formulation was introduced by Menter and developed especially for transitional flow, and it is usually combined with the $k-\omega$ turbulence model.

So, the $k-\omega$, $\gamma - Re_\theta$ turbulence model, apart from the two-equations of the $k-\omega$ model, have an additional two-equations system for the $\gamma - Re_\theta$ that are useful to solve the transition condition of the flow. This two-equation transition model introduces the intermittency factor (γ) that determines the percentage of time the flow is turbulent [14]

The transition phenomenon is solvable by the following two-equation system:

$$\frac{\partial(\rho\gamma)}{\partial t} + \frac{\partial(\rho U_j \gamma)}{\partial x_j} = P_\gamma - E_\gamma + \frac{\partial}{\partial x_j}\left[\left(\mu + \frac{\mu_f}{\sigma_f}\right)\frac{\partial \gamma}{\partial x_j}\right] \tag{2.15a}$$

$$\frac{\partial(\rho\overline{Re_{\theta t}})}{\partial t} + \frac{\partial(\rho U_j \overline{Re_{\theta t}})}{\partial x_j} = P_{\theta t} + \frac{\partial}{\partial x_j}\left[\sigma_{\theta t}(\mu + \mu_t)\frac{\partial \overline{Re_{\theta t}}}{\partial x_j}\right] \tag{2.15b}$$

This transition model was developed especially for modern unstructured CFD codes. For the case of some commercial software a correlation must be provided for the Free Stream Edge. Also, very often, some calibrations to this transition model must be conducted [15].

Using this transition model, particular attention must be paid to the dimensionless wall distance y^+.

In order for the viscous sublayer effect to be captured and the transition be properly modelled, the y^+ parameter must be small enough, generally $y^+ \leqslant 1$.

2.2.4 Spalart-Allmaras Standard Turbulence Model

The Spalart-Allmaras turbulence model is a one-equation model which solves the transport equation for the kinematic eddy turbulence viscosity ($\widetilde{\nu}$). It was developed mostly for aerospace applications and has gained popularity for turbomachinery applications. It has proven to be a good predictor for boundary layer flow with an adverse pressure gradient. The governing equation for this turbulence model is defined in equation 2.16.

$$\frac{\partial \widetilde{\nu}}{\partial t} + u_j \frac{\partial \widetilde{\nu}}{\partial x_j} = C_{b1}[1 + f_{t2}]\widetilde{S}\widetilde{\nu} + \frac{1}{\sigma}\left\{\nabla.[(\nu + \widetilde{\nu})\nabla\widetilde{\nu}] + C_{b2}|\nabla\widetilde{\nu}|^2\right\} - \left[C_{\omega 1} f_\omega - \frac{C_{b1}}{k^2} f_{t2}\right]\left(\frac{\widetilde{\nu}}{d}\right)^2 + f_{t1}\Delta U^2 \tag{2.16a}$$

Where the turbulence eddy viscosity ν_t can be written as a function of $\nu_t = \widetilde{\nu} f_{v1}$ and all the other variables can be written as a function of each other or are model constants. Refer to Appendix A.3 for detailed model equations

2.3 Composite Materials Concepts

Composite materials are composed by at least two constituent, different materials that present different behaviour when loaded and are chemically and physically different from one another. The combination of these materials is done having present the desired properties and behaviour of the final composite material.

Most composite materials are composed by a continuous phase material called matrix that binds together the reinforcement, usually in the form of fibers that can be either continuous or discontinuous and oriented or with random orientation.

The biggest advantage of using a composite material is the fact that it behaves according to the intended purpose. When combining two or more materials, the product fabric will combine the good characteristics of each of the composing materials. Figure 2.14 shows the stress-strain graph of the composite material and its components. It can be observed that the matrix has a clear plastic behaviour, while the reinforcement fiber has a solely elastic behaviour, with the association of these materials, a composite is created with a blended behaviour of its components.

Figure 2.15 presents three different kinds of Fiber Reinforced Composite (FRC): (a) oriented unidirectional fibers, (b) oriented multidirectional fibers and (c) is a composite with randomly oriented fibers. The properties of the composite material are dependent on the properties of the matrix, the properties of the fibers, the geometry of the fibers and their orientation. Composites with different fiber orientations will naturally behave differently.

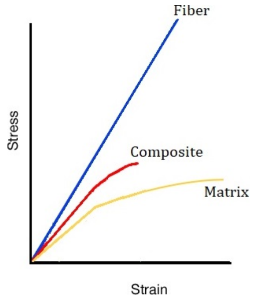

Figure 2.14: Strain vs. Stress graphic of a composite material and its constituents

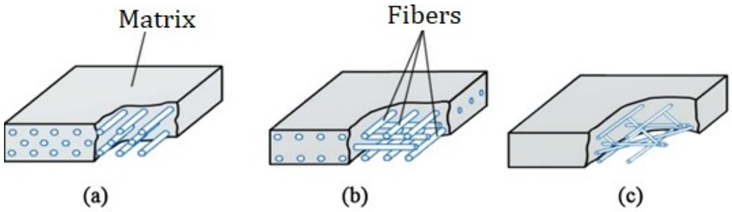

Figure 2.15: Three different composites with different fiber orientations

The most common composite material for maritime use is Fiber Reinforced Plastic (FRP). This composite material offers good resistance performance when compared with other materials. In the marine industry, this FRP has been widely used. From racing yachts construction to offshore oil platforms, the use of these composites offers many advantages over the use of steel, aluminium or wood, such as resistance to corrosion, ease of forming complex shapes and high specific material properties [16].
Manufacturing these FRP consists of a laminating process, laying up the fiber layers embedding them in a polymer binder or matrix and molding then into the Final geometry. This matrix is a bonding agent, usually a polymer liquid that cures (hardens) to a solid via a catalyst induced chemical reaction. When combined with the fiber reinforcement, it turns into a stiff material capable of sustaining high loads. In the mold, before starting plying the fiber layers and the resin, it is applied a material responsible to give high-quality finish to the visible surface of the composite, it is generally used a Gelcoat for this purpose. Figure 2.16 shows a carbon fiber component after the laminate process.

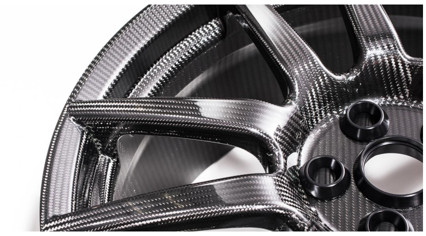

Figure 2.16: Carbon Fiber car wheel

2.4 Fin Design and Fluid Flow Properties

2.4.1 Windsurf Fin

The Windsurf Fin is a component of the windsurf board that is responsible for the directional stability and mainly responsible to counterbalance the sail side lift. A general representation of this aero-hydrodynamic balance is shown in Figure 2.17, this force diagram is a mere simplification of force balances acting on the overall set of board + sail + windsurfer. In this Figure, it is clear that the aerodynamic side force of the sail cancels with the hydrodynamic side force of the Fin, and that is the chief purpose of the Fin. In the case of this Windsurf Fin, the acting Lift force's direction is mostly horizontal, having an almost insignificant vertical Lift component due to the deflection of the Fin.

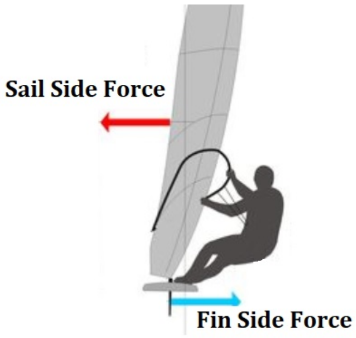

Figure 2.17: Sail and Fin balancing side forces

When sailing, the Fin is most of the times not parallel to the incoming flow, it is almost as if it is side slipping. This side-slip appears because the heading of the board is not the same as the course of sailing. The difference between these two directions is called the ”leeway” or ”drift” angle and is responsible for the angle of attack at the Fin, which, because it has a cross-sectional shape of an aerofoil, is responsible for the appearance of hydrodynamic forces that will balance with the aerodynamic forces on the windsurf sail. A schematic view of the mentioned concepts is presented in Figure 2.18.

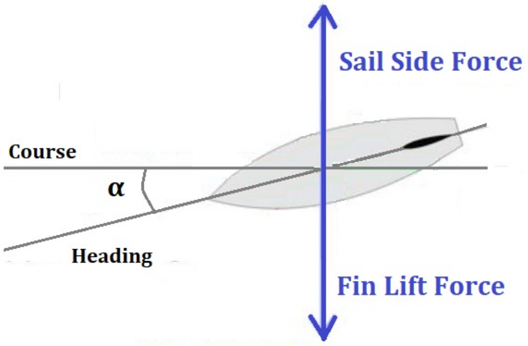

Figure 2.18: Representation of Fin's angle of attack and the most relevant aero-hydrodynamic forces

In this figure, the course direction is the same as the relative incoming flow direction and α is the drift angle, which can be interpreted as the angle of attack of the Fin.

Apart from the forces represented in Figure 2.18, there are still the aerodynamic forces on the sail responsible not only for the sail side forces but also responsible for the thrusting forces. Also, not represented, are the forces related to the board drag and lift and the force related to the weight of the sailor and the equipment.

As a simplification, to make easier for understanding, the aerodynamic sail forces were reduced to the sail side forces that match, in opposite direction, the lift forces on the Fin.

Like any other wing, the Fin can suddenly lose its lift, it stalls. It can happen when the angle of attack is bigger than the critical angle of attack. When sailing a windsurf, the AoA of the Fin generally does not go near or higher than the designed critical AoA. So, although it might happen, it is not very common for the Fin to stall due to high AoA. For the specific case of the profile of the Fin here studied, it stalls at an angle of AoA 8°, which is a value very uncommon for the practice of windsurfing in steady conditions. However, AoA bigger than this might appear when a gust hits the windsurfer or a wave causes a jump or dislocation to leeward, then a momentary value can be obtained above this critical AoA.

Some experimental tests were conducted at the Newcastle University's Emerson Cavitation Tunnel. Due to some testing restrictions, these were done for significant lower Reynolds number, but provided with significant data related to the critical angle of attack, concluding that stall would occur for AoA larger than 8°. Figure 2.19 shows the CFD (left) and experimental (right) data for the correlation of lift with the angle of attack. The CFD analysis was done for a Re: 5 x 10^5 [8] and the experimental test using a Re: 3 x 10^5 [17]. Despite the different Reynolds numbers, it is clear the decrease of lift force for AoA larger than 8°, which is a clear indicator for the appearance of stall.

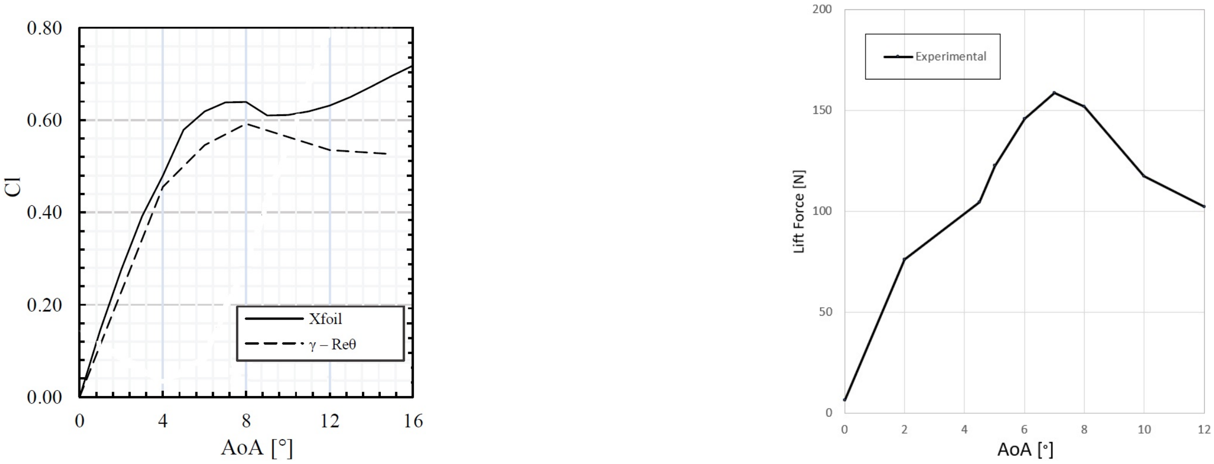

(a) Numerical analysis with Re: 5 x 10^5

(b) Experimental test Re:3 x 10^5

Figure 2.19: Lift and Lift Coefficient vs. AoA for numerical and experimental analysis

In Figure 2.19 (a), the results for 2 numerical simulations are presented, showing that both XFoil and Star CCM+ using the γ - Re_θ transition model have an agreement in relation to the critical AoA.

When sailing in unsteady conditions (usually when sailing in waves), and the board loses contact with water surface leaving the Fin partially submerged, this Fin can be characterized as a Surface Piercing Hydrofoil and as such, a way to lose stability of the board is when the low pressure on the surface of the Fin is sufficient to suck the air from the water surface so that the Fin stays involved by air, loosing completely its lift. This phenomenon is called Ventilation.

When the board loses all its sideways grip, it is commonly referred to as "Spin-out", and it happens due to 2 main reasons: Ventilation and high AoA Stall, being Ventilation the most common in practice.

2.4.2 F-Hot Slalom Fin

For this thesis, a Slalom Windsurf Fin is studied. This Fin is manufactured by F-Hot and has a 37 centimetres length, 10 centimetres chord at the base, 2.3 centimetres chord at the Tip and a rake angle of 2º to the aft. A general representation of the windsurf Fin studied in this work is presented in Figure 2.20 with all dimensions in millimetres and degrees.

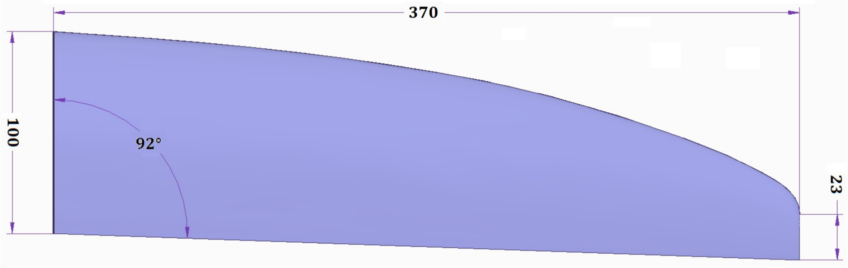

Figure 2.20: 37cm Windsurf Slalom Fin produced by F-Hot

The profile of the Fin is represented in Figure 2.21 and has a relative maximum thickness of 8.25 % of the chord and it is located at x/c=40.20 %.

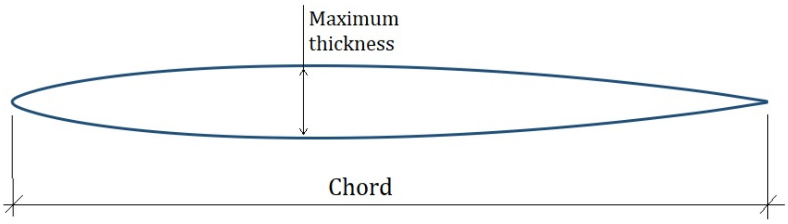

Figure 2.21: F-Hot Windsurf Slalom Fin profile

For the laminate process of this Fin, the reinforcement fibers used are carbon fibers and fiberglass, while the matrix is an Epoxy resin.

When laminating, the fibers are wet-laid up in the female molds in the form of a fabric. The fabrics used are Carbon Woven fabrics (interlaced fibers of carbon), Carbon UD fabrics (unidirectional fibers of carbon) and E-Glass UD (unidirectional fiberglass).

As the Fin is symmetric, plies are wet-laid up into both mirror sides of the mould which are then bolted together and the Fin thus cures as a single piece, avoiding potentially weak bond lines. On each side of the Fin, 19 layers of fiber fabric are laid and embedded with Epoxy resin. To produce these Fins, the laminating process is manual and therefore is not a fully controllable process, so the orientation of the fibers, as well as the amounts of resin used, might not be exactly the same for each Fin. For the case of these particular Fins, these differences are not significant and so every Fin is regarded as similar to each other and similar to the one numerically studied in the present work. The layup scheme for the laminating process is as follows:

- 3 layers of Carbon Woven fabric at about 45º in relation to the trailing edge

- 11 layers of Epoxy Carbon UD fabric at 0° with the trailing edge
- 5 layers of E-Glass UD fabric at 0° with the trailing edge

2.4.3 Fluid properties and operating conditions

The fluid flow used as working fluid for the simulations completed during the process of this work is seawater with a salinity of 35 g/kg [18].

The study of the Slalom Windsurf Fin was tested for some specific conditions, these conditions are presented in Table 2.1.

Parameter	**Value**	**Units**
Temperature (T)	20	° C
Density (ρ)	1024.9	kg/m^3
Dynamic Viscosity (μ)	1.077 x 10^{-3}	kg/m.s
Angles of Attack (AoA)	2, 4, 6	degrees
Velocity (v)	10, 15, 20, 25	knots
Average Chord ($\overline{c}$)	8.12	cm
Maximum average Reynolds number $(\overline{Re}_{max})$	0.9938 x 10^6	-
Minimum average Reynolds number $(\overline{Re}_{min})$	0.3975 x 10^6	-

Table 2.1: Operating Conditions for the simulations on the Windsurf Fin

The reason for the chosen angles of attack is because the values fall into the range of angles of attack where flow separation (stall) does not occur and are frequent drift angles when windsurfing. The velocities chosen are standard velocities for a Slalom Windsurf, it goes from 10 knots up to 25 knots, which is considered to be a reasonable average top speed at a Windsurf Slalom event. Accurate data for these slalom velocities is not widely available, so the top speed here considered is based on many riders' opinions and understanding of the sport.

Regarding the Reynolds number, as the Fin has a non-constant chord, each section will have a different Reynolds. To quantify this Reynolds number for each simulation, the average Reynolds number ($\overline{Re}$) is considered. To calculate the average Reynolds number, the concept of Aspect Ratio is used $\left[AR = \frac{b^2}{S} = \frac{b}{\overline{c}}\right]$. Knowing the surface area of the Fin to be $S = 300.46cm^2$ and the wingspan $b = 37cm$, it gives an average chord of $\overline{c} = 8.12cm$. With this value, the average Reynolds number was calculated for each simulation.

Additional conditions for which the Fin is numerically tested, are related to the fluid continua. The fluid is assumed to be an incompressible (constant density), steady and turbulent flow. All these conditions are then implemented into the CFD software for the numerical simulations.

Chapter 3

Hydrodynamic Model

3.1 Software used

During all the process of the hydrodynamic studies involved in this work, some commercial programs were chosen. During the verification and validation part of the project, XFoil was the selected software, while for the hydrodynamic study of the Fin, a more complex and versatile program was chosen, Star CCM+.

XFoil [19] is a simple interactive program used for the study of aerofoils. Uploading or choosing the aerofoil geometry and the characteristics of the flow around it, XFoil is able to calculate the pressure distribution, and therefore, the aerodynamic forces and the respective dimensionless coefficients acting on the aerofoil.

Star CCM+ [20] is a much more complete numerical simulation software focusing on Computational Fluid Dynamics (CFD) , able to study not only cases involving fluid flow but also heat transfer and structural stresses. It's an intuitive and easy to use program, and it comprises a Computer-Aided Design (CAD) modeler, a robust meshing generator, several models and parameters that can be tuned for the purpose of the analysis, such as the most commonly used turbulent models and the ability of a very powerful and intuitive post-processing analysis. The choice for the use of Star CCM+ came because of its availability and support at Laboratory of Fluid Simulation in Energy and Fluids (LASEF) in IST, but also because of its powerful simulation competences and its already known good performance when analysing turbulent fluid flow around wing-shaped geometries.

3.2 Validation Process

The Validation process is of the utmost importance to be able to assess the level of confidence that should be attributed to a CFD simulation. The credibility of CFD results for both academic research and industry-level purposes is only obtained if a concrete and well-defined verification and validation plan is set forth. Therefore, for this work, verification and validation of the computational results is required in order for it to be scientifically reliable.

With the final purpose of validating the CFD model on Star CCM+, two studies were conducted using both commercial software, following some verification and validation methodologies [21]. These validation processes include:

1. XFoil validation with experimental data
2. Choice of modeling parameters

3.2.1 XFoil Validation

The validations of the XFoil software is done comparing data from Xfoil against experimental data. For this process, the following parameters were reproduced.

Aerofoil	NACA 012
Validating parameters	C_l and C_d
Reynolds Number	1 x 10^6

Table 3.1: XFoil Validation parameters

The aerofoil NACA 012 was chosen because of its similarity to the cross-section of the Windsurf Fin here studied, and also because of the availability of experimental data for this geometry at a Reynolds similar to the maximum Reynolds used for the final study of the Fin. Some good parameters to validate the XFoil results are the lift and drag coefficients. The experimental data was provided by aerodynamic tests in a wind tunnel in Sandia National Laboratories [22].

A study for the drag and lift coefficients was done to compare the XFoil and the experimental data, the results are as follows in Figure 3.1.

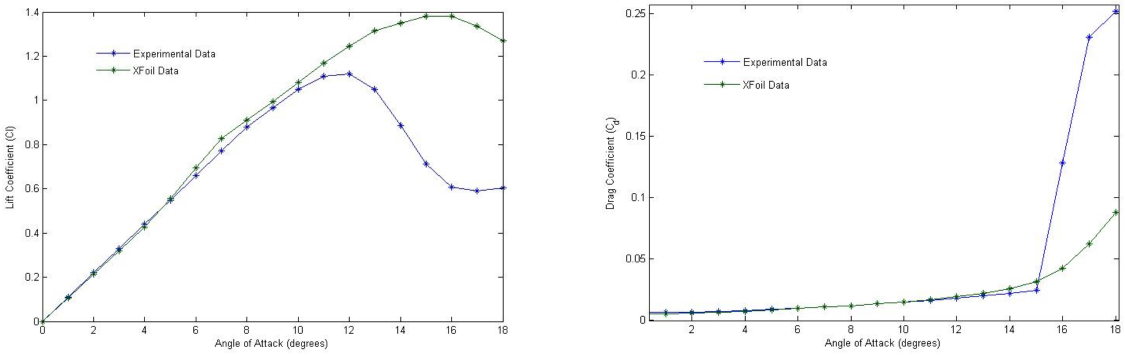

(a) Lift Coefficient vs. AoA

(b) Drag Coefficient vs. AoA

Figure 3.1: Comparison between XFoil and Experimental Data for NACA 012 aerofoil

Analysing the graphs of Figure 3.1, it is possible to conclude that the results obtained by XFoil are in agreement with the experimental data up until an angle of attack of about 12°. It is also legitimate to assume that the critical angle of attack falls into the range of angles of attack where the data from XFoil and experimental tests start do diverge from one another (critical AoA of about 12°). The main reason for these divergences in values of C_l and C_d is due to the fact that XFoil is not a very good predictor for separated boundary layer flow, having some inconsistencies when compared with experimental values. It can be concluded that the results obtained by XFoil are valid for angles of attack below the angle for which stall occurs. As the AoA used for the final study of the Fin are inferior to the critical AoA, the results from XFoil can be used for comparison purposes when selecting the modeling parameters to be used in the hydrodynamic analysis of the Fin.

3.2.2 Choice of modeling parameters

For this analysis, the outcome will be the choice of the most adequate turbulence model and discretization parameters to be used in the hydrodynamic study of the Fin. To do so, the following simulation parameters were selected:

Aerofoil	NACA 0008-34
Analysed parameters	C_l and C_d
Reynolds Number	1×10^6
Angle of Attack	2°

Table 3.2: Parameters for the choosing and validation of mesh and turbulent model

The NACA 0008-34 aerofoil selected is extremely similar to the profile of the Fin studied (refer to section 2.4.2), with a maximum relative thickness of 8 % located at x/c = 40 %. The Reynolds number used is the same as the maximum Reynolds used for the final study of the Fin.

In this analysis, an aerofoil is numerically simulated and the results of Star CCM+ will be compared with the XFoil results, previously validated, in order to decide on the most adequate turbulence model and discretization parameters.

So, to decide both on the mesh parameters and the turbulence model to be used, a grid sensitivity study is required for each of the different turbulent models.

The turbulence models that will be considered are the same ones previously presented in section 2.2: $K-\epsilon$, $k-\omega$ SST, $k-\omega$ $\gamma-Re_\theta$ and Spalart-Allmaras.

Regarding the mesh, a decision was taken not to use the Law of the Wall (as described below). This decision was supported by the work of Firooz [23] that stated that when using turbulent models in low Reynolds simulation (about Re $<$ 2 x10^6), the agreement with experimental data will be enhanced if the boundary layer is numerically solved without wall law.

The wall law defines the velocity profile of the flow in a fully turbulent boundary layer and is applicable to the parts of the flow that is closest to the wall, Figure 2.11 presents the dimensionless velocity profile in this region.

Ideally, to properly define the flow inside the boundary layer, the first cell from the wall should lie within the very thin viscous sub-layer. Though this might be possible for certain flow scenarios, this criterion cannot be satisfied for complex flows in complicated geometries as it would require a very fine mesh resolution near the wall which would widely increase the time required for solving the problem. The wall law comes to solve this problem, it calculates the flow in this near-wall region without the need for such a fine mesh. Generally, when using wall laws, the first mesh cell from the wall can be at $30 < y+ < 300$. So, when not using the law of the wall, a finer definition of the mesh in the near-wall region is required in order for the whole boundary layer to be properly captured. This better resolution of the mesh will increase the simulation time but at the same time, will enable a good prediction of the boundary layer flow. Not using this wall law, implies that the first mesh cell from the wall must be significantly nearer the wall surface, generally $y^+ < 1$. In the Star CCM+ software, not to consider the wall law means that a Low y+ wall treatment is chosen for the simulations.

3.2.2.1 Mesh Parameters

All the numerical computational simulations in this work are done using Star CCM+ CFD software, where the flow is numerically solved using the Finite Volume Method (FVM). This FVM consists on discretizing the computational fluid domain, dividing it into several smaller volumes where the governing Equations 2.11 can be applied.

Base size

For all the simulations, the base size was set as an absolute value, all the other dimensions were set as a relative dimension to the base size (except for the prism layer thickness), so if the base size decreases, all the other parameters also decrease, increasing the number of grid cells, which leads to a better flow discretization and consequently minor numerical errors.

Prism Layers

In order to capture the boundary layer, prism layers are used. This prism layers control one of the most important parameters, the y^+ value, responsible to guarantee that the boundary layer, especially the viscous sub-layer has enough cells to be resolved in a proper way. The prism layer thickness should have at least the dimension of the boundary layer thickness, so in order to estimate this value, a correlation for a turbulent boundary layer flow over a flat plate was used:

$$\delta = 0.37 \cdot c \left(\frac{1}{Re} \right)^{-1/5} \tag{3.1}$$

For the case of the maximum average Reynolds number considered on this work, 1x10^6, which is the case considered in this selection process, and a chord length (c) of 0.1m, the estimated boundary layer thickness is δ = 0.00233m. Since this is only an estimation, it is reasonable for the prism layers thickness to slightly differ from this value. For this specific case study, a prism layer thickness of 2 mm was chosen. The height of the first cell from the wall (ΔS) is calculated as follows:

$$\Delta S = \frac{y^+ \mu}{\rho \cdot u_\tau} \tag{3.2}$$

Where μ is the dynamic viscosity and u_τ is the friction velocity given by equation 2.6. The number of prism layers is also a parameter that will define the grid definition near the wall. Having too much prism layers will increase the mesh refinement and will require much more computational time and resources. Having enough prism layers is very important when not using wall laws due to the need of having several layers in each different zone of the boundary layer, so that each of these zones is discretized independently. A representation of the prism layers is shown in Figure 3.2

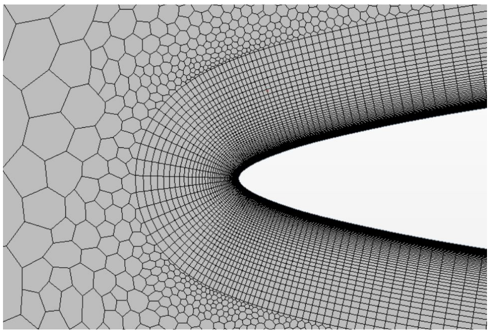

Figure 3.2: Prism layers around aerofoil leading edge

Computational Domain

The computational domain chosen for this study is a 2D quadrangular domain with a length of 10 times the aerofoil's chord and a height of 8 times the chord. Two volumes of refinement (VOR1 and VOR2) were implemented to give a higher mesh definition near the tested aerofoil. In Figur 3.3 a representation of this domain is presented.

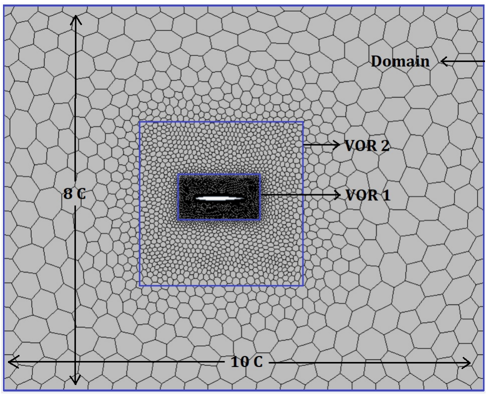

Figure 3.3: Computational Domain with Control Volumes

Tested Meshes

Four different meshes were tested for this grid refinement analysis. For each of the used meshes, a grid characteristic number is associated. This characteristic number, r_i, is given by:

$$r_i = \sqrt{\frac{h_1}{h_i}} \tag{3.3}$$

Where h_1 is the number of cells in the most refined grid and h_i is the number of cells in grid i.
In table 3.3, the most important characteristic parameters of the four different mesh grids are presented. These parameters are the most important ones in regards to the mesh resolution.

Char. Number (r_i)	**Number of cells (h_i)**	**Base size [m]**	**PL Thickness**	**Number of PL**
$\mathbf{r}_4$ = 1.737844	29899	0.05	0.002	30
$\mathbf{r}_3$ = 1.253668	57453	0.05	0.002	60
$\mathbf{r}_2$ = 1.116716	72409	0.05	0.002	80
$\mathbf{r}_1$ = 1	90298	0.03	0.002	80

Table 3.3: Grid sets for numerical calculations of four different turbulence models

Apart from these parameters, the custom size for the Surface Mesher of the VOR 1 and 2 also differ for different meshes, having smaller cell sizes for the finer meshes.

3.2.2.2 CFD Grid Convergence analysis

To estimate the uncertainty of a CFD simulation, there are various methods. The one here chosen, is a grid refinement study introduced by Roache [21].
For an angle of attack of 2 degrees, the Lift and Drag Coefficients (C_l and C_d) were calculated for each of the 4 turbulent models and each of the meshes previously detailed. Having calculated the values for the C_l and C_d and comparing them with XFoil data, it is possible to calculate the uncertainty between the Star CCM+ and XFoil values and decide on the most adequate parameters to be used in the hydrodynamic model.
The numerical uncertainty, U, is associated to the use of a certain grid i and is defined by:

$$U = F_S \cdot |\delta_{RE}| \tag{3.4}$$

Where F_S is a safety factor assumed as 1.25 and δ_{RE} is the error estimation which is solely a discretization error, meaning that round-off errors and iterative errors are negligible. This error estimation is given by equation 3.5:

$$\delta_{RE} = \phi_i - \phi_0 \tag{3.5}$$

Where ϕ_i is the numerical solution of any scalar quantity on a given grid i (in this case C_l and C_d). and ϕ_0 is the estimated exact solution.

The ϕ_0 is analytically interpreted as the numerical solution of a mesh with r_i=0, which is the same thing as saying a mesh with infinite cells. To calculate the ϕ_0, after plotting the ϕ_i vs. r_i, a linear interpolation is made between every single ϕ_i, resulting in a straight line with the linear equation $y = mr_i + b$. The parameter b is the value at which the interpolation line intercepts the y-axis and corresponds to the estimated exact solution ϕ_0.

Knowing ϕ_0, the numerical uncertainty of each grid can be calculated (eq. 3.4) as well as the range of values where the numerical solution can variate, i.e. the uncertainty interval (eq. 3.6):

$$\text{grid } i \text{ numerical solution} \in [\phi_i - U, \phi_i + U] \tag{3.6}$$

To compare the numerical results from Star CCM+ and XFoil results, there are two things to be checked. First, verify for each grid if the XFoil result is inside the range of numerical uncertainty. And second, calculate the relative error between the estimated solution and the XFoil solution. This relative error is given by equation 3.7:

$$\text{Relative Error} = \frac{|\phi_0 - \phi_{XFoil}|}{\phi_{XFoil}} \tag{3.7}$$

At the end of this analysis, depending on the C_l and C_d relative error for each of the turbulent models, the most adequate model will be selected. And also, if all the grids present a small range of numerical uncertainty, it is fair to say that the solution is mesh independent for the meshes analysed.
The Lift and Drag coefficients are the parameters here used to compare the numerical and XFoil data. The XFoil values for these variables are: C_l(XFoil) = 0.2107 and C_d(XFoil) = 0.0047.

Numerical results using k-ϵ, Standard Turbulence model

Char. Number (r_i)	**C_l**	**C_d**
r_4 = 1.737844	0.215255	0.012851
r_3 = 1.253668	0.215384	0.012742
r_2 = 1.116716	0.215919	0.012759
r_1 = 1	0.213098	0.012649

Table 3.4: Numerical results for k-ϵ TM for the 4 different mesh grids

Interpolating the results for C_l and C_d, the estimated exact solution, ϕ_0, is then calculated and gives: C_l (ϕ_0) = 0.2129 and C_d (ϕ_0) = 0.0125.
For each of the grids, the numerical uncertainty is calculated via equation 3.4. In Figure 3.4, the values for the C_l and C_d and its uncertainty ranges are exhibited.

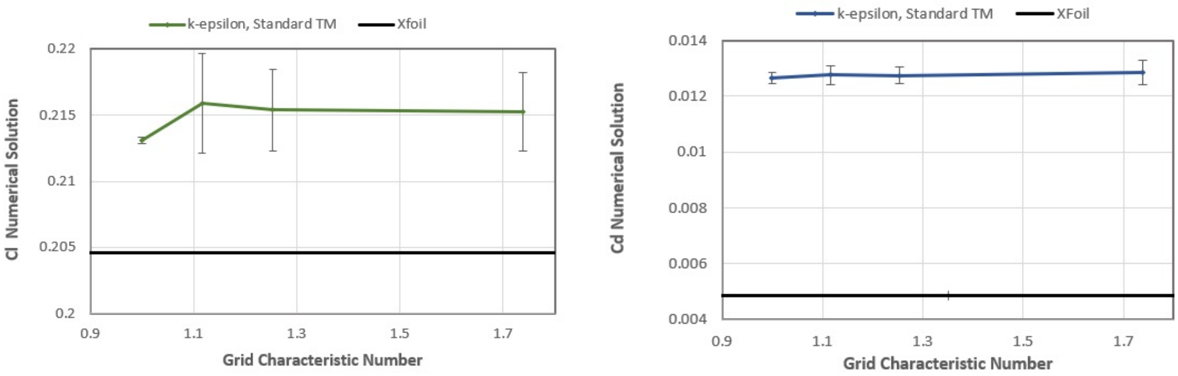

Figure 3.4: Numerical results for C_l (left) and C_d (right) using k-ϵ TM

Numerical results for k-ω SST Turbulence model

Char. Number (r_i)	**C_l**	**C_d**
r_4 = 1.737844	0.218259	0.011072
r_3 = 1.253668	0.218911	0.010973
r_2 = 1.116716	0.219247	0.01096
r_1 = 1	0.216208	0.010826

Table 3.5: Numerical results for k-ω SST TM for the 4 different mesh grids

The values for the estimated exact solution are: $C_l(\phi_0)$= 0.2166 and $C_d(\phi_0)$= 0.0106. The uncertainty range is calculated and shown in Figure 3.5 along with the numerical solutions of each of the meshes.

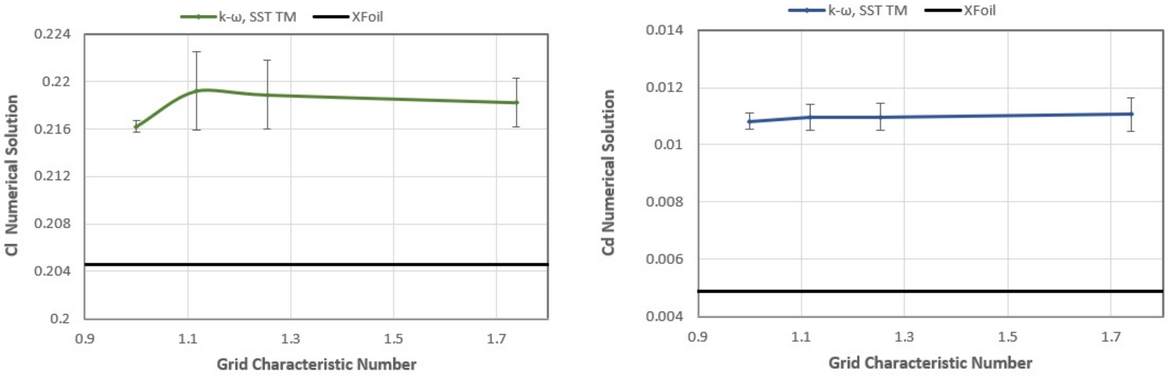

Figure 3.5: Numerical results for C_l (left) and C_d (right) using k-ω SST TM

Numerical results for k-ω SST, γ - Re_θ Turbulence model

Char. Number (r_i)	**C_l**	**C_d**
r_4 = 1.737844	0.21909739	0.0050353
r_3 = 1.253668	0.21631838	0.0049771
r_2 = 1.116716	0.21825241	0.0049682
r_1 = 1	0.2142525	0.004846

Table 3.6: Numerical results for k-ω SST, γ - Re_θ TM for the 4 different mesh grids

The estimated exact solution of the aerodynamic Coefficients are $C_l(\phi_0)$= 0.2107 and $C_d(\phi_0)$= 0.0047. Note that for this turbulence model, not only the C_l is similar to the one calculated by XFoil, but also, the C_d has a good agreement with XFoil data, which did not happen for the other turbulence models. Apart from the similarity in the results of C_l and C_d, another interesting thing to observe is the fact that for every single mesh, the XFoil result falls inside the uncertainty interval of each simulation.
Figure 3.6 shows the numerical results for each of the grids and also their uncertainty range.

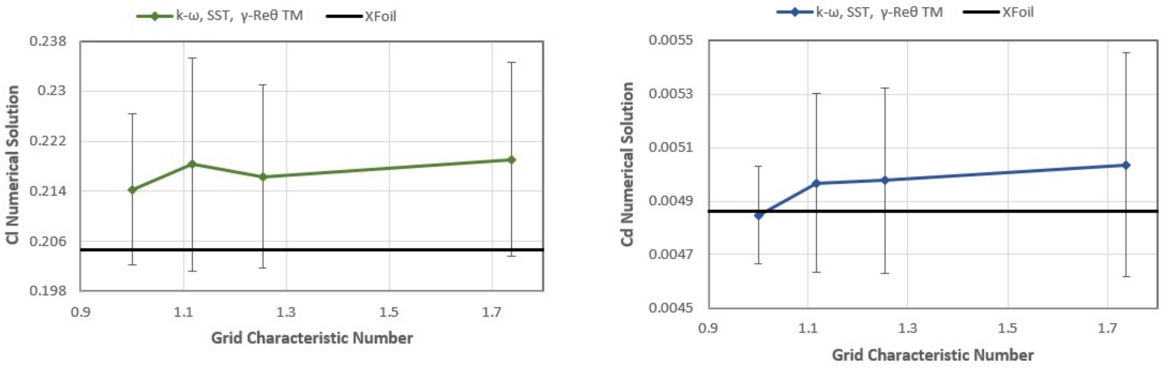

Figure 3.6: Numerical results for C$_l$ (left) and C$_d$ (right) using k-ω SST, γ - Re$_\theta$ TM

Numerical results for Standard Spalart-Allmaras Turbulence model

Char. Number (r$_i$)	**C$_l$**	**C$_d$**
r$_4$ = 1.737844	0.2196381	0.011041
r$_3$ = 1.253668	0.2199019	0.010943
r$_2$ = 1.116716	0.2207136	0.01091
r$_1$ = 1	0.2177747	0.010782

Table 3.7: Numerical results for Spalart-Allmaras TM for the 4 different mesh grids

For this last turbulence model, the estimated exact solutions are C$_l(\phi_0)$= 0.2181 and C$_d(\phi_0)$= 0.0105. Figure 3.7 presents these results as well as the uncertainty range and the XFoil obtained values for C$_l$ and C$_d$.

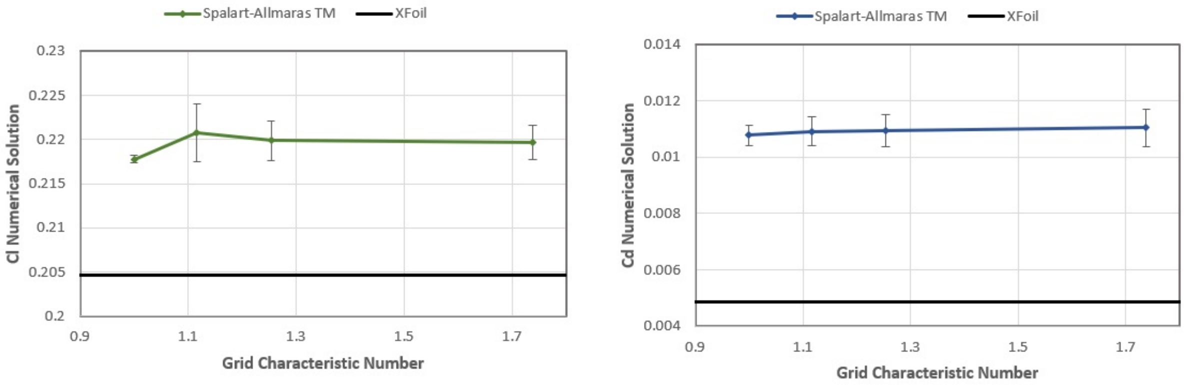

Figure 3.7: Numerical results for C$_l$ (left) and C$_d$ (right) using Spalart-Allmaras TM

Conclusion

Looking at the previously presented data, we can observe that the only turbulence model that present adequate results when compared with XFoil data is the k-ω, γ - Re$_\theta$ turbulence model. This turbulence model presents considerable small uncertainty intervals for both aerodynamic coefficients, and at the same time, the XFoil results are all inside these intervals (Figure 3.6).

To support the choice for the k-ω, γ - Re$_\theta$ turbulence model, the relative errors were calculated for each of the turbulence models for both aerodynamic coefficients and presented in Table 3.8.

k-ϵ, SST	C_l	4.05 %
	C_d	157.20 %
k-ω, SST	C_l	5.87 %
	C_d	118.11 %
k-ω, SST, γ-Reθ	**C_l**	**2.98 %**
	C_d	**3.29 %**
Spalart-Allmaras	C_l	6.60 %
	C_d	116.05 %

Table 3.8: Relative Error for the four studied Turbulence models

In general, all turbulence models have a relatively small error in the lift Coefficient but present a far too large relative error in the drag coefficient (except for the k-ω, SST, γ-Re$_\theta$ model). This can be explained by the fact that the boundary layer is being modeled as fully turbulent and therefore, it is neglecting a large laminar part (characteristic of a low Reynolds number flow). So, when using the γ-Re$_\theta$ transition variant, which is a good transition predictor, it captures the laminar part of the flow decreasing the errors of the drag coefficient.

The chosen k-ω turbulent model is a very common model to calculate transition from laminar to turbulent, as explain by Eça et al. [24], compared with other eddy-viscosity models, the k-ω model shows a fairly good agreement with the expected results. The γ-Re$_\theta$ variation of the k-ω turbulent model was proven by Sørensen [25] to give promising numerical results with outstanding agreement with experimental data, being an excellent predictor for Lift, Drag and the transition point.

The results of the studied uncertainty of each turbulent model as well as the work of the two previously mentioned authors, give a high level of assurance for the use of the k-ω turbulent model with the γ-Re$_\theta$ transition model for the CFD study of the Fin.

Regarding the mesh parameters, a conclusion was drawn that all the turbulence models present a small uncertainty interval, and this means that the results are marginally independent of the mesh refinement, which means that no matter how refined the mesh is, it will give solutions very similar to the ones of coarser meshes. The mesh parameters that were chosen were the ones of the coarsest mesh, because, using this mesh discretization, not only it gives agreeable results with XFoil data, which was previously validated with experimental data, but also it does not compromise very much the computational demand of the problem.

3.3 CFD Process

The Windsurf Fin study to be conducted, is a 3D analysis of the referred component. This analysis starts with a Computational Fluid Dynamics (CFD) study that must be performed following some guidelines. Next, are presented the most important steps to be followed:

Geometry:

The first thing to do when starting a CFD analysis, is to create the CAD model. Star CCM+ has the capabilities of CAD designing. In the case of this specific work, the CAD model is designed in Solid Edge and then imported into Star CCM+. The fluid domain is a quadrangular prismatic volume with the Fin geometry in the middle of it. Figure 3.8 represents the fluid domain of the problem.

Boundary conditions:

Then, it's advised to name the surfaces, in order to facilitate of process of choosing the type of boundary condition. After that, each named surface must be assigned to a region and be identified with a type of boundary. In the study of the Windsurf Fin, the boundary conditions used are: *Velocity Inlet* for the inlet surface and the side surfaces, *Pressure Outlet* for the outlet surface, and *Wall* for the Fin surface. Figure 3.8 shows a representation of these boundary surfaces where the side surfaces are the ones perpendicular to the Inlet and Outlet and are also defined as *Velocity Inlet*.

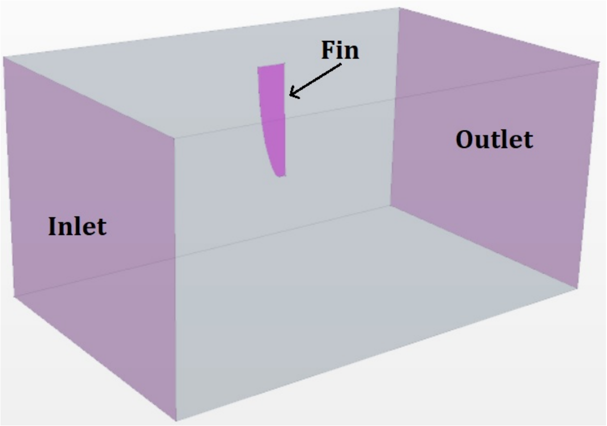

Figure 3.8: 3D Computational Fluid Domain and Boundary Surfaces

Mesh

The mesh is created using the *Automated Mesh* feature of Star CCM+, with the characteristics of the grid chosen in the validation section **??**. For the generation of the fluid domain's discretization, the used Meshers were: *Surface Remesher*, *Polyhedral Mesher* and a *Prism Layer Mesher*. The mesh to be used in all the CFD simulations has the following main characteristics presented in Table 3.9.

Base Size	0.05 m
Number of Prism Layers	30
Prism Layer Thickness	0.002 m
y^+	< 1
Domain relative cell size	150 %
VOR 1 relative cell size	8 %
VOR 2 relative cell size	50 %

Table 3.9: Final mesh main parameters

In some cases, the relative cell size of the Volumes of Refinement (VOR) was slightly changed due to convergence issues. Figure 3.9 shows a cross-section of the 3D discretized fluid domain, it can be observed the similarities with the 2D mesh chosen in section 3.2.

In general, all the 3D simulations here performed, respecting the mesh parameters previously stated, are composed of about 3 million cells, maintaining a good mesh definition especially in the near-wall region. This mesh is a significant improvement in relation to a mesh generated for the same computational volume in a previous work [8] that was composed of 11 million cells, which was much more computationally demanding.

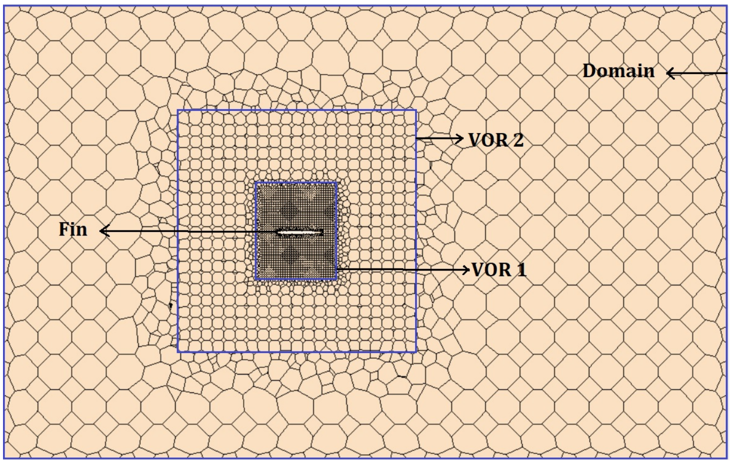

Figure 3.9: Mesh Discretization of 3D Computational Fluid Domain

Physics Continuum properties

Before running the simulation, the physical properties of the problem must be set. After validating the Turbulent model and deciding not to use the law of the wall, the physics continuum models defined for all the Fin simulations are:

- Three-Dimensional analysis
- Steady and Segregated flow
- Constant density (incompressible)
- Turbulent flow solving the Reynolds-Average Navier-Stokes equations
- K-ω, SST (Menter) Turbulence model
- γ-Re$_\theta$ Transition model
- Low y+ Wall Treatment (no Wall Law)

Solution Convergence

The convergence of the numerical results is an extremely important part of the simulation process. To know a converged solution was reached, two criteria can be used: Residual values and the analysis of a specific quantity of interest.

Residual values are one of the most fundamental measures of an iterative solution's convergence, as it quantifies the error in the solution of the governing system of equations. In an iterative numerical solution, the residual will never be exactly zero. However, the lower the residual value is, the more numerically accurate the solution. For CFD purposes, residual levels inferior to 10^{-4} are already considered a loosely converged solution (Figure 3.10 (a)).

Another way to check solution convergence is to analyses the evolution of a specific quantity over the various iterations. In a steady state analysis, for a converged solution, the numerical results between iteration i and iteration $i + 1$ should be negligible or even null. So, in order to check convergence, it is possible to monitor the evolution of some specific quantities and check if there is a negligible solution variation between consecutive iterations (Figure 3.10 (b)).

For the specific study of the Windsurf Fin, the convergence criteria used were the two previously mentioned ones: convergence of the residuals and convergence of the Lift solution. Figure 3.10 shows the monitors of a converged solution for a Fin with 6° AoA and at 25 knots of velocity.

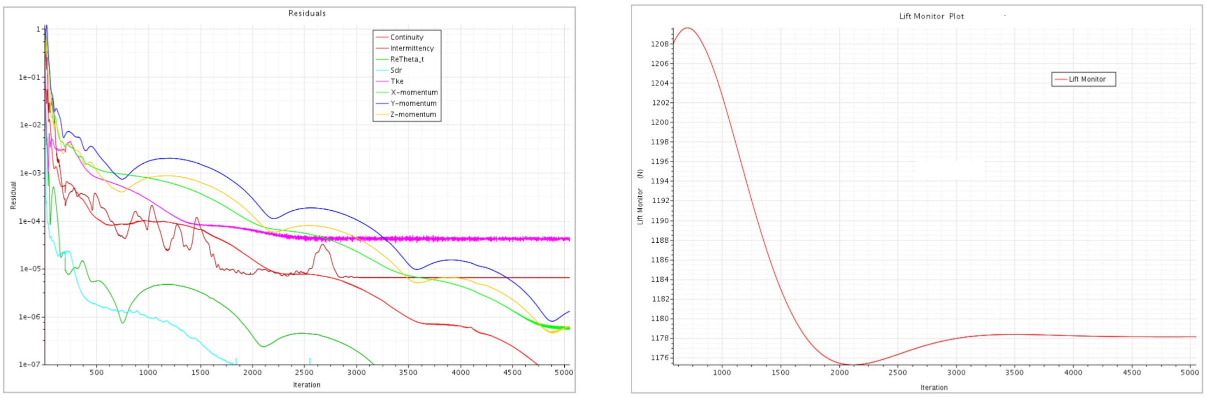

(a) Residual values convergence

(b) Lift monitor convergence

Figure 3.10: Satisfied convergence criteria for a converged solution

For some simulations, the solution did not satisfy the convergence criteria, in these cases, to reach a converged solution, a small refinement of the mesh was done near the Fin's surface. Also, another practice that proved very effective to arrive at a converged solution, was to change the Relaxation Factors (RF), changing the velocity RF to 0.5, the pressure RF to 0.1 and the turbulence RF to 0.5.

The Relaxation Factor is a coefficient frequently used in iterative solvers. When solving iterative nonlinear equation systems, it can happen that the solution starts to diverge. In these cases, a RF is used to help the solution to stabilize and to get to converged results. For that, the RF is used, using the results of iteration i and $i - 1$ to define the value that should be used for the next iteration $i + 1$.

Using relaxation methods is often interpreted as if applying a ”smoothing filter” to the numerical solutions that present a tendency to diverge. Figure 3.11 presents a representation of the iterative process' results, showing a divergent progress and a convergent progress that uses the manipulation of RF.

Under-Relaxation ($f <$ 1) of a CFD simulation reduces the solution oscillations and helps to keep the computation stable. Although being a good way to arrive at a converged solution, using under-relaxation factors generally causes an increase of computation time.

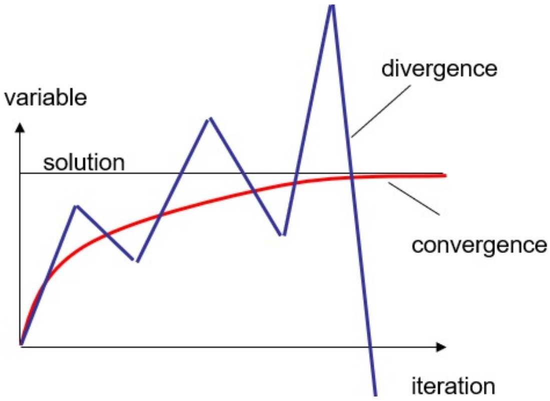

Figure 3.11: Divergent and convergent progress of an iterative process

Post-processing;

Finally, to be able to make conclusions about the finished simulations, a post-processing analysis is done. Star CCM+ has a very powerful and simple post-processing feature. In the case of the present work, the post-processing analysis consists of visualizing streamlines and other color mapped data that capture the tip vortex, laminar separation bubbles, turbulence intensity, pressure distribution and other interesting scalars. The central parameter used in the present work that is obtained while post-processing, is the pressure distribution on every element on the Fin's surface, which is then used for the Structural part of the project. Two examples of a post-processing outcome can be seen in Figure 3.12, where the pressure distribution over the fin's surface and a Laminar Separation Bubble are presented.

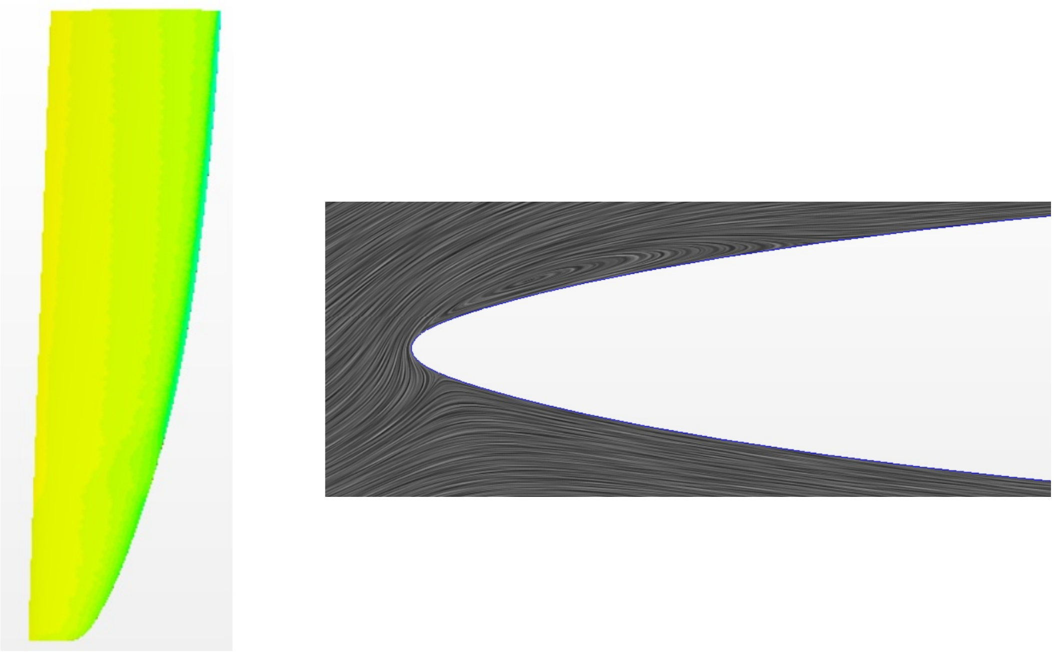

Figure 3.12: Visualization of results of pressure distribution (left) and Laminar Separation Bubble (right) of a Fin simulation at 20 knots and 6^o AoA

Chapter 4

Structural Model

After the CFD analysis of the Fin, the pressure distribution induced by the water moving around the Fin's surface was calculated and is then imported into the structural analysis to assess how the component behaves when hydrodynamically loaded.

The structural model here presented is based on a previously developed model [6]. A reconstruction of this model was conducted in order to be able to import the proper CFD loads into the structural analysis. To create this model, the Fin manufacturer provided a lay-up scheme describing the fabrics to be applied and their respective locations and orientation. A virtual model of this structure was constructed based on these data provided by F-Hot.

4.1 Software Used

The structural part of this project was all developed using the ANSYS software that, despite also having the capabilities to solve fluid flow problems, it was solely selected to perform the structural analysis.

The laminating process on this software uses a module named ANSYS Composites PrepPost (ACP) which allows the user to specify the layers properties, stacking-up sequence and orientation and decide upon other specifications that enable the creation of the virtual composite material that behaves in a similar fashion to the actual Fin's material.

4.2 Model Calibration

The calibration of the structural model and the first characterization of the numerical laminate composition was conducted by Nascimento [6] in a previous work focused on the same Windsurf Fin.

As the composite laminating process is a manual labor, the construction precision is not extremely exact, so, when creating the numerical model of the laminate, there is some margin for changing the physical properties and lay-up of the plies, in order for the numerical results to match experimental ones. To do so, a calibration of this structural model is done.

Calibration and validation of the developed numerical model is achieved using experimental methods,

mechanically testing the Fin using a mechanical servo-hydraulic test machine and a real scale Fin provided by the F-Hot Fin manufacturer. A simple point loading was used to allow a comparison between the FE model results and the experimental ones.
The mechanical tests consisted in applying a point load at the hydrodynamic centre of pressure, at about a quarter of the chord from the leading edge. The tests were performed at 40 % and 80 % of the Fin span which is where the centre of pressure of a semi-elliptic loading generally is. Figure 4.1 shows a representation of the experimental set for both point loading tests.

(a) 40 % of the Span

(b) 80 % of the Span

Figure 4.1: Experimental set for point loading analysis at 40 % span (left) and 80 % span (right) [6]

When experimentally testing the Fin, the hydraulic cylinder controlled by a computer and installed perpendicular to the Fin's surface, causes a displaces to the Fin at a rate of 0.1 mm/s to simulate a static loading. When deflecting the Fin, the probe is systematically calculating the force being exerted and the respective deflection caused, then being able to plot the force-displacement behaviour of the Fin (Figure 4.2). The Fin behaves in a linear manner, which means that the Fin is only operating in the elastic domain, which verifies the composite material theory presented in section 2.3.

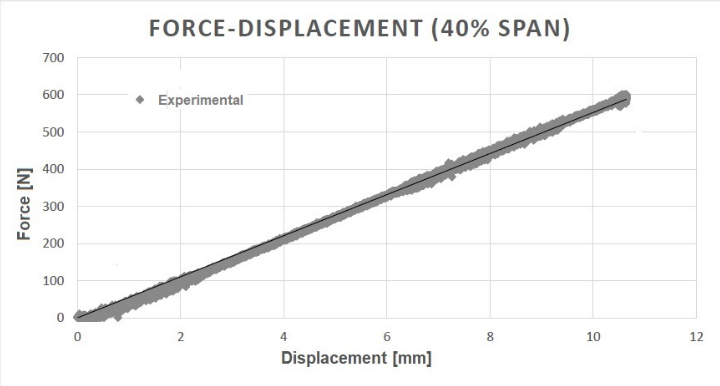

Figure 4.2: Force-Displacement behaviour of the Fin loaded at 40 % of the span

After collecting data for the deflection induced tests on two different points of the Fin, a comparison with the ANSYS analysis using the initial structural model is done. After verifying that the results for the load at 40 % of the span do not match the numerical simulation results, a calibration procedure is introduced.

The numerical simulation results also verify the elastic behaviour of the material, but with the results presenting a different slope for the stress-strain performance. So, the calibration process will focus on the main parameter responsible for the material's behaviour in the linear-elastic domain, the Young's Modulus (E). For this calibration, an iterative process is conducted, readjusting the Young's Modulus of the composite elements in order for the numerical results to match the experimental ones. After a series of adjustments to E, the properties of the laminate constituents were set, building a final virtual structural model that behaves similarly to the experimental tests, Figure 4.3 shows the comparison between both agreeing results on a force-displacement graph.

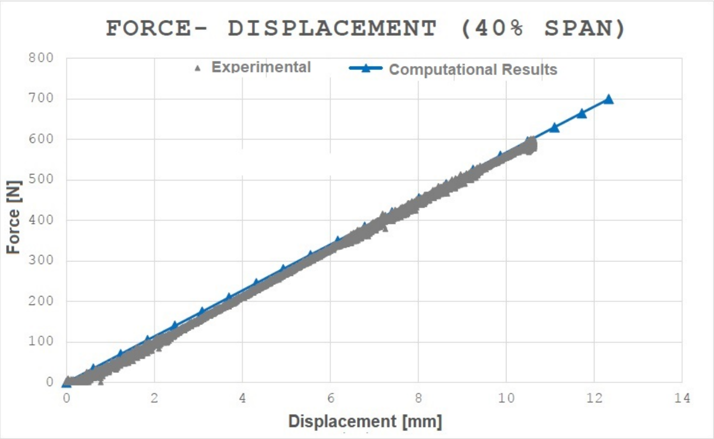

Figure 4.3: Force-Displacement behaviour comparison between Experimental and Numerical results

4.3 Structural Analysis Process

The structural analysis of the Windsurf Fin is performed in the ANSYS Workbench, where a series of different system blocks are placed, each of them with a specific purpose. For the case of a single analysis of the Fin, the structural model block diagram created is as shown in Figure 4.4.

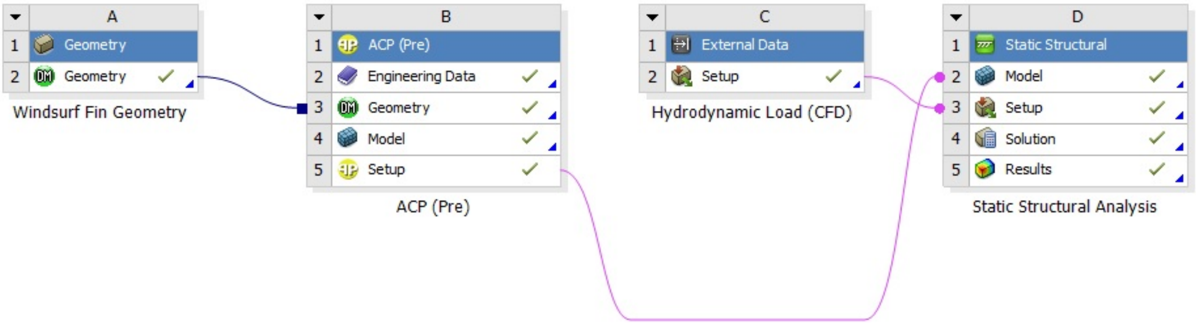

Figure 4.4: Diagram for the Structural analysis on ANSYS Workbench

The structural analysis process starts with the geometry that must be imported from an external CAD designing software into block A. For the CAD modeling, Solid Edge was used
After, in the ACP (Pre), block B, the numeric laminating process is done. Here, the composite material lay-up scheme, assembly of the fabrics and every physical property of the material is defined. It is also in this block that the FE model is created and the mesh is automatically generated. ACP (Pre) provides a good visualization tool of the laminate, being able to see each layer of fabric as well as a color mapped representation of the Fin's thickness along its surface. Figure 4.5 presents the outcome of this ACP (Pre) model.

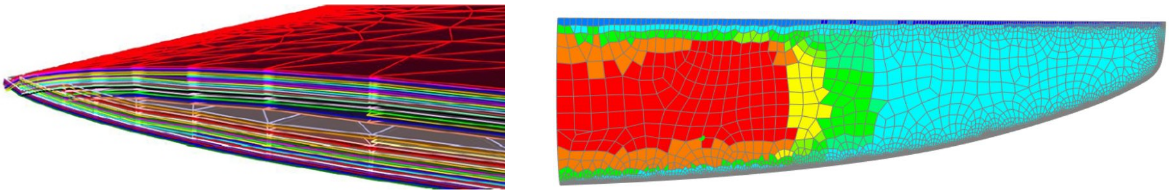

Figure 4.5: Representation of the numeric composite laminate

Block C is an External Data system, where the CFD hydrodynamic pressure load is imported. After the CFD results are obtained in Star CCM+, the pressure on every mesh cell is obtained and exported to a spreadsheet with the location and pressure value on each cell. This spreadsheet is then imported into ANSYS Workbench via block C that in its turn will perform a mapping of the spreadsheet data onto the Fin's surface mesh, appointing a pressure value to every mesh cell.
Finally, in block D is where the structural analysis is done. Here, the geometry and composite laminate properties are imported from block B and the pressure load is imported from block C. Apart from this, the boundary conditions must be set, in this case is a fixed support at the Fin's base and the pressure load acting on the Fin's surface. These boundary conditions can be seen in Figure 4.6

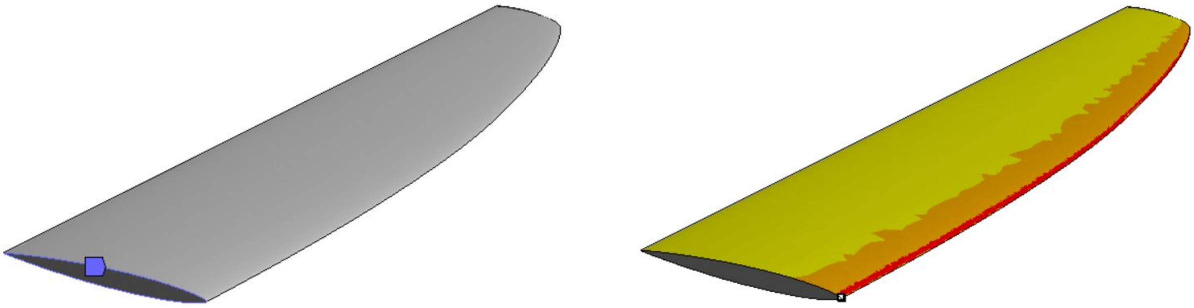

(a) Fixed Support on the base of the Fin

(b) Mapped pressure load distribution on the Fin's Surface

Figure 4.6: Boundary Conditions applied to the Fin

After running the simulation, several results can be evaluated. For the analysis of the Fin, the main solution parameters to focus on are the Fin deformation and the total force acting on the Fin (equal in value to the reaction force on the fixed support). Figure 4.7 shows the deformation and the reaction force on a Fin being operated at an AoA of 6° and 20 knots of velocity. In this structural analysis, the maximum deflection occurs at the Fin tip's trailing edge and is 7.6 cm and the hydrodynamic force in the direction perpendicular to the incoming flow (Lift) is about 750 N of force.

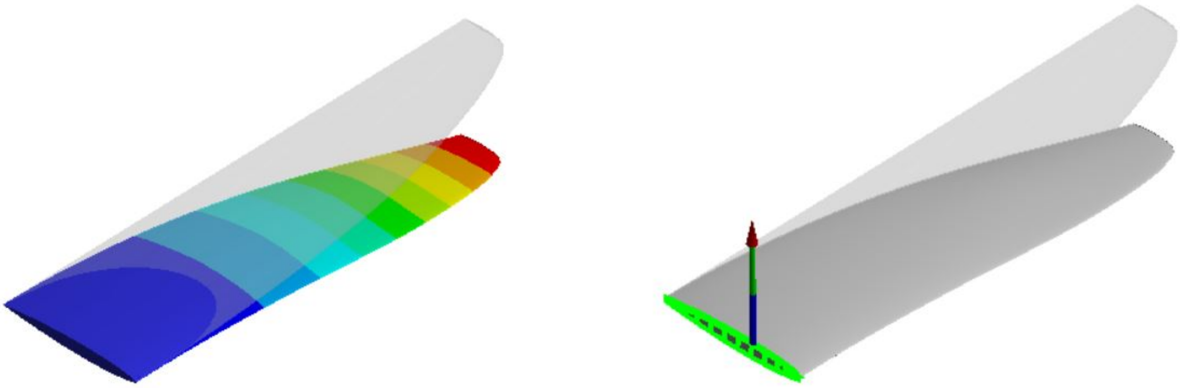
(a) Fin's Deformation

(b) Fin's reaction force at the fixed support

Figure 4.7: Visualization of the numerical simulation solution of the F-Hot Slalom Windsurf Fin

It is possible to extract the deformation value of any node of the mesh, namely the deformation of the leading and trailing edge at the Fin tip. Knowing these values, is then possible to calculate the twisting of the Fin tip (evaluated at a plane at 36 cm from the Fin's base) and take a conclusion about its twisting behaviour for different loading conditions.

ANSYS Workbench also offers the possibility of a good post-processing analysis, using the ACP (Post) system. It is possible to study the cracking of the laminate, examine each layer and each mesh element individually and predict failure modes. As the material failure analysis is not of interest for the present work, the ACP (Post) system will be disregarded.

Chapter 5

Fluid-Structure Interaction Model

The Fluid-Structure Interaction (FSI) is a process that studies the interaction between a deformable structure and an internal or surrounding fluid. The FSI analysis consists on the coupling between the laws that describe fluid dynamics and structural mechanics. This interaction can be either static or oscillatory. In the case of the present work, this interaction is a stable one characterized by a constant flow around a Windsurf Fin, that, depending on the material properties and flow pressure and velocity, will have a deformation associated to this fluid-structure interaction.

This kind of analysis is of extreme importance in multiple engineering fields, being very important to properly define the behaviour of a solid structure immersed in moving fluid flow. The case of oscillatory FSI analysis is often crucial for designing considerations, failing to consider the effects of oscillatory interactions can be catastrophic. For the present work, the analysis of the Windsurf Fin, will solely consider a stable FSI analysis. An oscillatory analysis would be an interesting topic for a future work focused on the same Fin.

A FSI analysis was proposed for this work due to the need of a more exact prediction of the structural behaviour of the Windsurf Fin when in operation. In the previous studies of this Fin [8] [7], a structural analysis of a 3D Windsurf Fin was done using a pressure load obtained by extrapolation of the results from a 2D hydrodynamic study. This is considered to be a One-Way FSI, where the hydrodynamic loads are firstly calculated and then imported into a structural analysis. In this case, a single iteration was performed.

Making a single iteration FSI study provides with a fair estimate of the structural response, but to study the response with greater accuracy, Multiple Iterations must be conducted because, after the first iteration, the deformed geometry will constitute a new boundary for CFD calculation, which will result in different pressure loadings, hence the need for Multiple Iterations until the difference of hydrodynamic loads between iterations is negligible.

The present work proposes an FSI model that performs a Multiple Iterations FSI analysis, in order to predict with higher accuracy the structural behaviour of the Windsurf Fin.

5.1 Software used

Throughout all the process of creating a Multiple Iterations FSI model, two main software were used. For this type of analysis, a flow solver and a structural solver must be used and coupled together.

Using the previously presented software on Chapters 3 and 4, Star CCM+ was selected to do the hydrodynamic study, while ANSYS Workbench was used for the structural analysis.

Despite having these competencies, a decision was made not to use ANSYS Workbench to perform all the FSI analysis, but only used for the structural part. This is because of the excellent performance of Star CCM+ in CFD studies and also because of license limitation that does not allow for a decent grid refinement on ANSYS. So, two different commercial software were used for the creation of the FSI model.

Apart from the CFD and Structural software, a CAD software (Solid Edge) was also used to perform geometry treatment between iterations. Also, Excel was extremely useful to make the link between Star CCM+ and ANSYS Workbench, being useful for the import and export of the pressure loads.

5.2 Limitations and Decisions

There are two ways of developing this FSI model: manually or in an automated way.

To do the automated process, an Application Program Interface (API) should be developed, which is responsible to automatically do the connection between the CFD and Structural software. This API is composed of a set of routines that sends specific commands to the simulation software, eliminating user interference during simulations. To automate this process, the ANSYS Mechanical APDL (ANSYS Parametric Design Language) should be used instead of ANSYS Workbench. Getting familiar with the creation of an API and developing the automated processes would be extremely time consuming and would ultimately compromise the final work results due to less time dedicated to the simulations. So, a decision was made, from the beginning of this work, to manually make the coupling between the CFD and the Structural parts of the project.

Another major factor that conditioned the work done was the available ANSYS license. When using ANSYS Workbench, the ANSYS student license was used, and so, certain limitations were constant during the whole project. The most significant limitation when using the student license was the numerical limitation, namely the maximum number of mesh cells allowed in a simulation.

For the case of a CFD simulation, the maximum allowed number of elements are 512,000 Nodes/Cells, and this was one of the reasons why the CFD analysis was not done on ANSYS, because, the license limitation did not allow for a good mesh refinement which would compromise the CFD final results.

As for the Structural simulations, the maximum allowed number of elements is 32,000 Nodes/Elements. When doing a Multiple Iterations FSI analysis, after a structural analysis, the deformed geometry must be transferred to the CFD software for the next iteration simulation with the deformed geometry (refer to section 5.3 for FSI process). When exporting a deformed geometry from ANSYS, the outcome is the

geometry of the mesh, so, because of deficient mesh resolution, it generates an uneven surface, with the possibility of sharp edges.
As the ANSYS' ability of mesh refinement is not adequate with a student license, when exporting the deformed geometry, the surface will present a lot of sharp edges, especially in the leading edge. So, because of this license numerical restriction, a direct transfer of geometry from ANSYS to Star CCM+ is highly not recommended and a geometry treatment is of extreme importance before the CFD analysis in order for it to give adequate results. Figure 5.1 shows the Fin's leading edge before and after a geometry treatment.

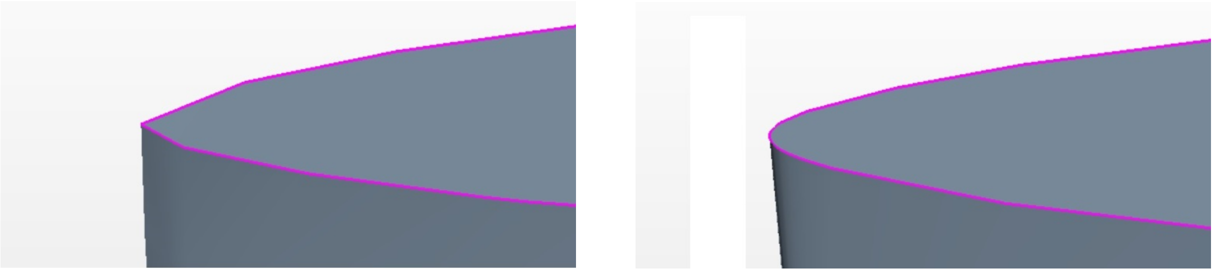

Figure 5.1: Leading edge representation before (left) and after (right) geometry treatment

The necessary geometry treatment before importing into the CFD Software is another reason why a manual approach to the development of the FSI model was chosen, because automatically performing this geometry treatment in Solid Edge would be virtually impossible.
Despite the process being extremely time-consuming and all these limitations and restrictions faced during this project, certain decisions were made, and all the issues were solved in an efficient manner that did not compromise the results nor the simulations initially planned out.

5.3 FSI Process

One of the major objectives of the present work is to develop a Multiple Iteration Fluid-Structure Interaction model capable of doing the FSI analysis in an efficient way. Despite the previously mentioned restrictions, a model was created generating reasonable and reliable results.
The FSI analysis is an iterative and dynamic process of coordinating the hydrodynamic and structural analysis. All this process is done using Star CCM+ and ANSYS Workbench. Star CCM+ is used solely to perform the hydrodynamic studies which will generate some data to be later imported into ANSYS Workbench. ANSYS is not only used for the structural study of the Fin, but also, it's there where the consecutive iterations are done and organized into ANSYS' diagram blocks.
In Figure 5.2, a simplified diagram can be seen, showing the consecutive actions required for this Multiple Iterations FSI analysis.

A representation of the FSI model diagram blocks on ANSYS can be seen in Figure 5.3. In this Figure, each line represents one iteration, only three iterations are presented here.

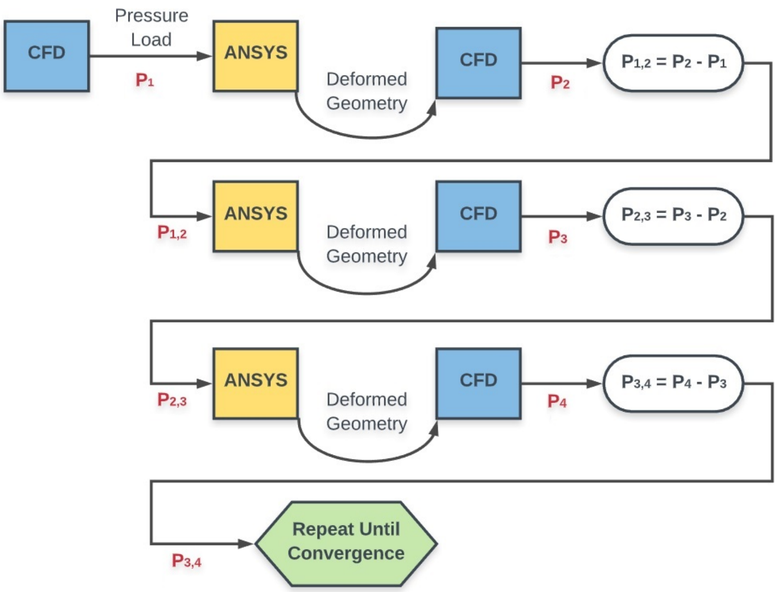

Figure 5.2: Multiple Iteration FSI model process diagram

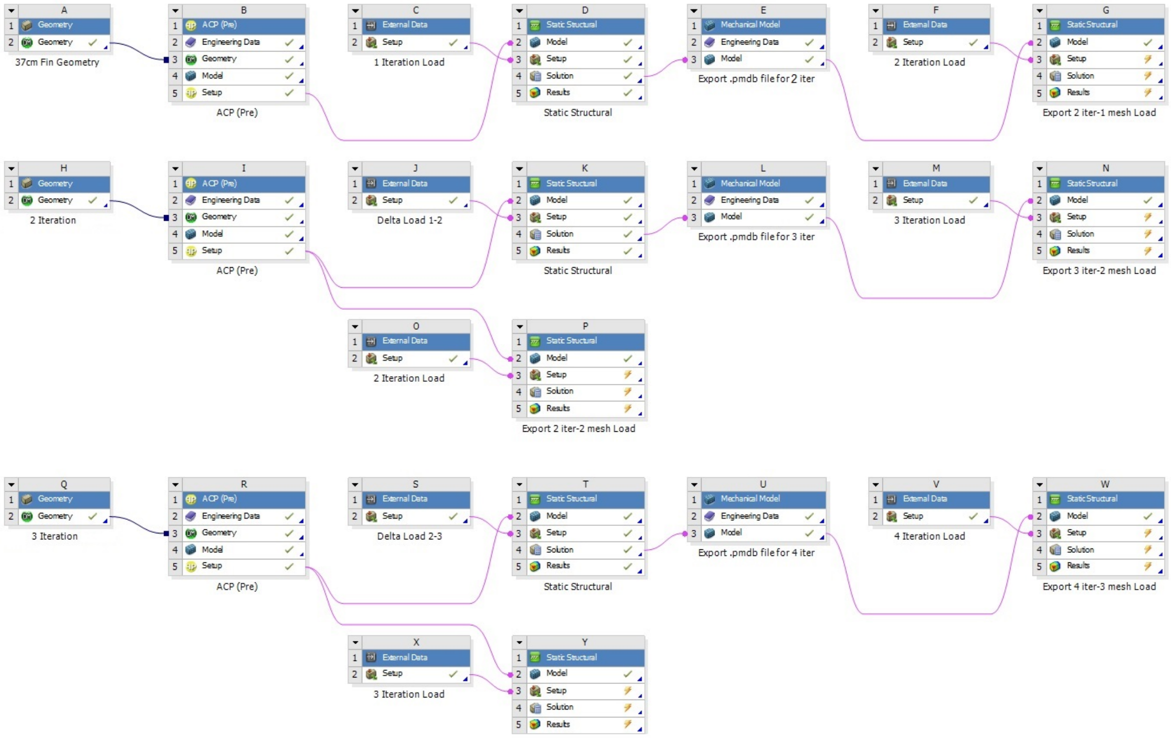

Figure 5.3: ANSYS block diagram of the Multiple Iteration FSI model

Similar to the Structural model previously presented (Chapter 4), all the ACP (Pre) blocks (B, I and R) are the systems responsible for generating the mesh, create the virtual laminate and assign the composite material to the Fin. And all geometry blocks (A,H and Q) are the systems where the CAD geometry is imported.

The process starts with the numerical hydrodynamic analysis of the undeformed Fin on Star CCM+. From this simulation, the data important to calculate is the pressure load on each of the Fin's surface mesh and their respective coordinate location. To obtain this data, a scalar plot is created on Star CCM+

showing the pressure on the Fin's Surface along the 3 cardinal directions. Figure 5.4 shows the pressure distribution on the Fin's surface along these three different directions x, y and z.

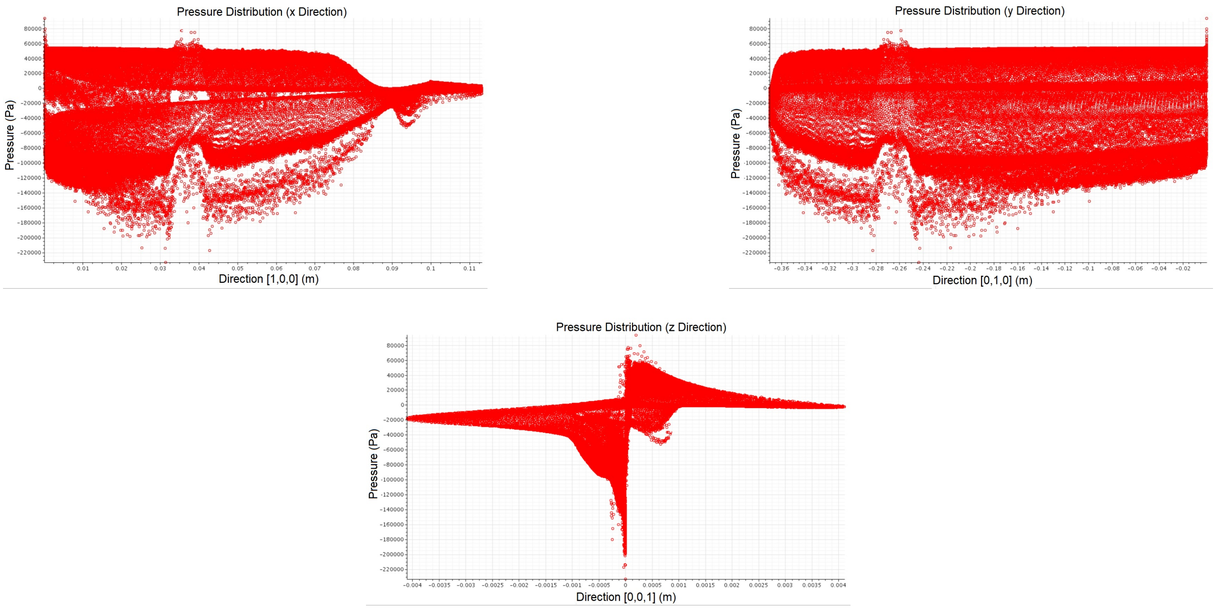

Figure 5.4: Pressure Distribution along X, Y and Z axis on a Fin at 20 knots and an AoA of 4°

From these graphs, it's possible to export to a spreadsheet the coordinates of each of the surface mesh elements and their hydrodynamic pressure caused by the relative water flow around the Fin. This pressure load data (P_1) is then imported into the FSI model to proceed with the structural study. The hydrodynamic load is imported into block C which is then associated to block D to serve as boundary condition for the first structural analysis.

The next block (E) is responsible to Export the deformed geometry to be then imported again into the CFD software for the next iteration hydrodynamic analysis. But because of license limitations, a direct transfer from ANSYS to Star CCM+ is not advisable and a reconstruction of the deformed geometry is done on a CAD software. To perform this geometry treatment, a mapping of several points of the Fin's base, tip, leading and trailing edge is done and imported into Solid Edge, where splines passing through these points are drawn and the fin is then reconstructed with a smooth surface and without sharp edges. Figure 5.5 shows the splines of the Fin's base, tip leading and trailing edge before full reconstruction.

Figure 5.5: Fin outline for the geometry treatment procedure

After reconstructing the deformed geometry, it is imported into Star CCM+ for a second hydrodynamic analysis, in order to calculate the second pressure loads on the Fin's surface (P_2).

After having calculated this P_2 Load, it will be analysed the difference between this pressure distribution and the initially calculated one (P_1), to check if, between these iterations, the load converged. To do so, the Δ Load is calculated and a structural analysis with this Δ Load is done to check the reaction of the structure to this Δ Load. Ultimately, in order to get an FSI converged solution, the difference between the hydrodynamic loads of two consecutive iterations must be negligible.

The reason why a Δ Load is applied for each structural analysis, is because these analyses are done to the already deformed geometries, so, what is being studied here is the Fin's deformation associated with the difference between loads of 2 consecutive iterations.

So, for each iteration of the FSI analysis, the pressure load to be used must be equal to the difference between the last two hydrodynamic loads ($P_{i-1,i}$ = P_i - P_{i-1}). This Δ Load can be used, due to the linear-elastic structural behavior of the Fin's composite material.

For the second FSI iteration, in order to check convergence, the load applied will be the difference between the first and the second hydrodynamic loads, $P_{1,2}$ = P_2 - P_1. So, the second pressure distribution load (P_2) is again imported into ANSYS into the next blocks (F and G). These blocks' main purpose is to, together with block D, calculate the Δ Load ($P_{1,2}$) to be applied to the second FSI iteration. In block K, it's possible to observe the deformation is much smaller than before, because it is actually the Δ Deformation corresponding to the applied Δ Load $P_{1,2}$

The proceeding actions are similar to the already done. This process will continue for as long as there is a significant deformation of the Fin. To know when to stop the iterative process, some convergence criteria were defined.

Convergence Criteria

To know when to stop the iterative process, it was defined a convergence criterion, which is the maximum allowed Lift force difference between iterations in relation to the Lift force of the first iteration. The convergence criterion created follows equation 5.1:

$$\Delta L = \frac{|L_{i-1} - L_i|}{L_1} < 2\% \tag{5.1}$$

Also, for convergence to be achieved, a maximum deflection on the last iteration was imposed, this deflection must be below 4 millimetre (twice the Tip's maximum thickness) in order for the FSI process to be considered converged. The choice of the 4 mm maximum value to consider the process converged, is because of natural oscillations of the Fin's Tip when steadily sailing. These oscillations could reach values near twice the tip's maximum thickness (from observation of water tunnel tests), that is why the choice for this 4 mm deflection convergence criterion. Despite these small oscillations, this Fin's analysis is still considered a static study due to the minor magnitude of these fluctuations.

5.3.1 FSI Case Study

For exemplification purposes of the FSI model, two specific cases will be focused on: A Fin at 20 knots of velocity and an AoA of 4° and another extreme case of a Fin at 25 knots and an AoA of 6°. For both cases, the FSI analysis required different number of iterations and both met the convergence criteria.

In these analyses, special attention will be given to the Tip deflection of each iteration, the Lift force convergence and the variation of the twist angles throughout the iterations.

Velocity 20 knots, AoA 4°

For this specific case, the FSI simulation arrived at a converged solution after 5 iterations, this means that five different CFD and structural simulations were needed to capture a more precise behaviour of this Windsurf Fin sailing in these specific conditions.

In Figure 5.6 are presented the Lift force, the ∆ Tip deflection between consecutive iterations and the progress of the Tip Twist angle for each of the 5 iterations.

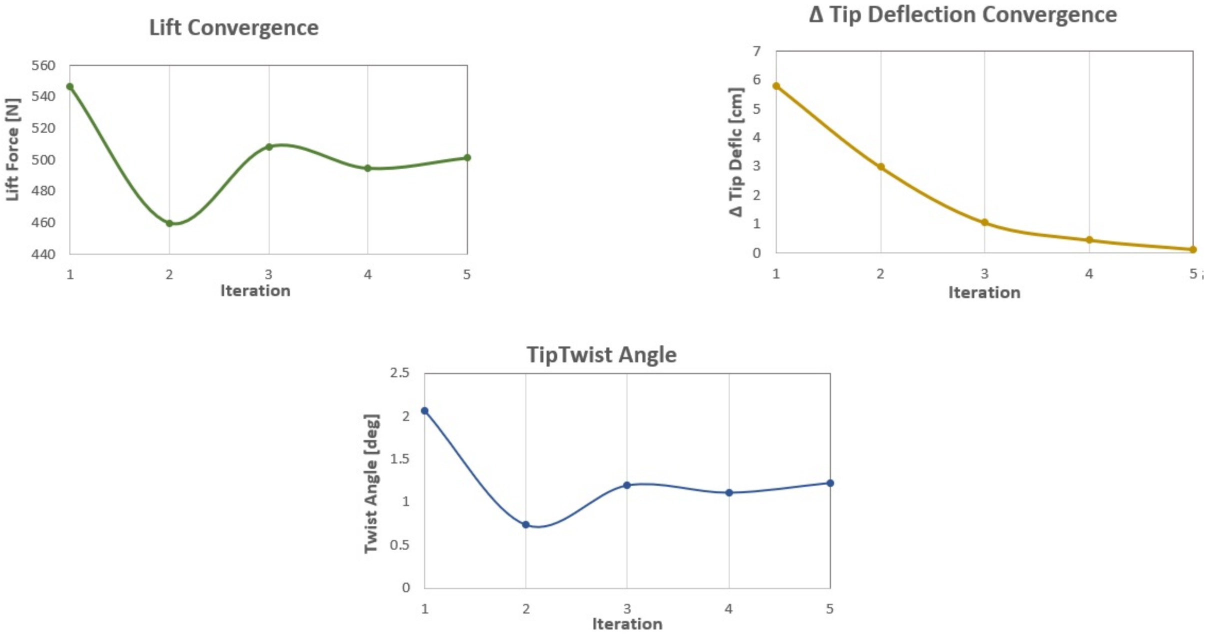

Figure 5.6: FSI solutions monitor for 3 parameters for conditions of 20 knots and AoA 4°

The convergence criteria are satisfied here, with a final relative ∆ Lift of 1.2 % in relation to the first iteration value and a final ∆ Deflection of 0.13 cm in the last iteration. Regarding final values, the Lift is 500.86 N, the maximum total Tip Deflection is 3.65 cm and the final Tip Twist is of 1.2°.

Velocity 25 knots, AoA 6°

Unlike the other case study, in this FSI simulation, a converged solution was obtained after 10 Iterations. This is because of much larger deformations of the Fin, which leads to a bigger difference of results between iterations and consequently, the need for more simulations to arrive at a final result.

In this case, comparing it with the previous one, there is an increase of the angle of attack to 6°, together with an increase of velocity to 25 knots, so it is expected for the hydrodynamic loads to be more intense and consequently, the Fin's structural behaviour be also more expressive. Figure 5.7 shows the evolution of the same three parameters along the 10 iterations.

Also, in this case study, the convergence criteria are satisfied, with a final relative ∆ Lift of 0.67 % in relation to the first iteration value, and a final ∆ Deflection of 0.24cm. The final results for these three

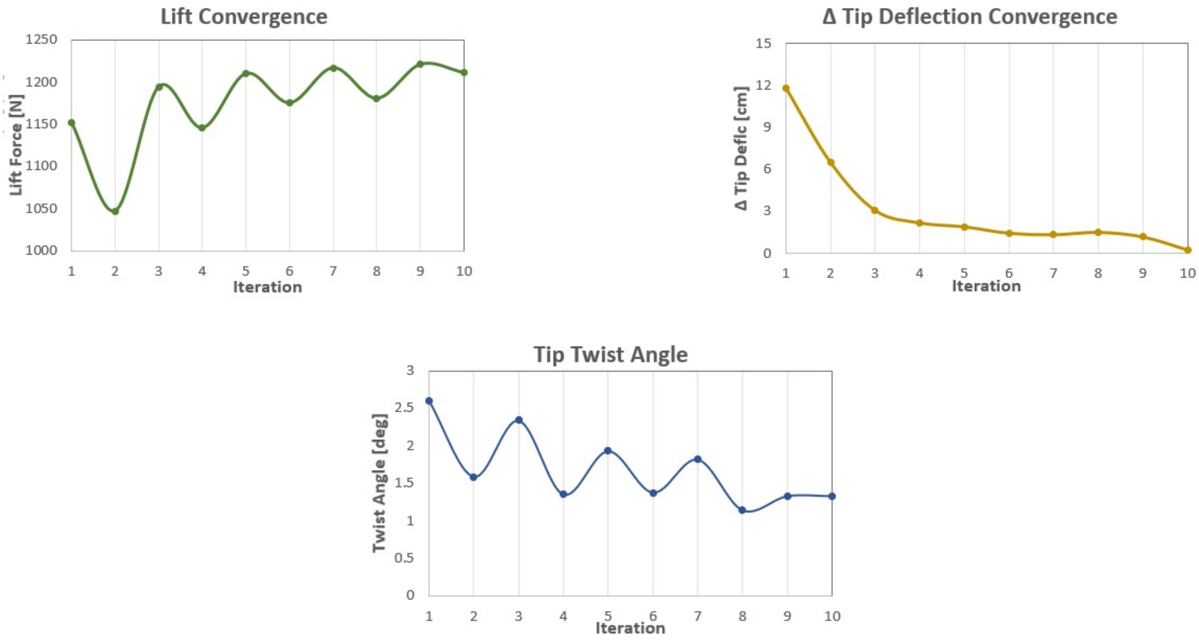

Figure 5.7: FSI solutions monitor for 3 parameters for conditions of 25 knots and AoA 6°

parameters are a Lift Force of 1210.7 N, a total maximum Tip Deflection of 8.05 cm and a final Tip Twist angle of 1.3°.

Conclusion

These are only 2 examples out of the 12 FSI analysis completed during this project, and looking at the monitor plots for the 3 parameters, it can be observed that a solution convergence was reached.
For the convergence criteria, the Lift and Deflection parameters were purposely selected for being the most interesting parameters to investigate and the ones that converged faster.
The choice for not using the Tip Twist angle as a convergence criterion is because it takes much longer to converge, because it is both a very small and a very sensitive parameter, which means that it fluctuates a lot with slight load changes. Also, because of successive geometry treatments and various structural analysis causing deflections on every mesh element, the calculation error of this Tip Twist angle might be considerable. In some of the cases simulated, the Tip Twist angle did not arrive at a converged solution, and this is mainly because of the already explained natural oscillations of the Fin's Tip allied to the sensitivity of the Twist angle parameter. This can be explained by physical phenomena such as the appearance of a Laminar Separation Bubble (LSB) in the vicinity of the Leading edge and its dimension variation between iterations. This topic will be further analysed in the following Section 6.3.
So, due to this Twist fluctuations and convergence issues, it was decided for further analysis to consider the Tip Twist angle calculated in the first iteration, the same as if not using the developed FSI model. This decision, in these two case studies, despite presenting fairly converged solutions for the Tip Twist, would cause twist differences reaching up to 40.5 % and 49.0 % respectively, making this simplification for the Tip Twist angle calculation only acceptable to identify trends and orders of magnitude and not absolute values for this parameter.

Chapter 6

Results and Discussion

After several FSI analyses for each of the proposed cases in Table 2.1: Velocity of 10, 15, 20 and 25 knots and an AoA of 2°,4° and 6°, some conclusions start to be drawn in regards to the Fin's behaviour when in operation. These conclusions and observations are in regard to 3 main parameters:

- Lift Force
- Fin Deflection
- Fin Twist

The first parameter to be analysed is the Lift Force, which is the hydrodynamic force acting on the Fin perpendicular to the incoming flow. The two other parameters are related to the structural behaviour of the Fin when hydrodynamically loaded. These last two parameters are generally coupled together and referred to as the bend-twist effect, but here these concepts will be dissociated and separately considered. In Figure 6.1, a representation of the Fin's behaviour is shown. Here, it can be seen the deflection and the twist of the Fin provoked by the hydrodynamic forces generated by the moving fluid flow around it.

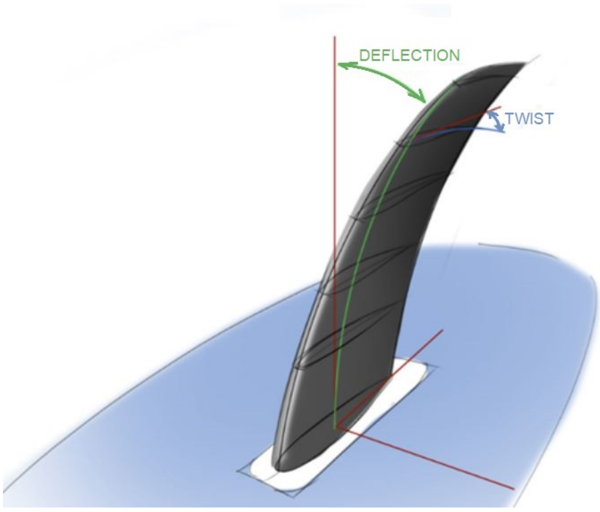

Figure 6.1: Fin's structural bend-twist behaviour

6.1 Lift Force

The Lift force here evaluated is the most significant hydrodynamic force acting on the Fin. It is the component of the resultant force which is perpendicular to the exterior flow direction. When steadily sailing without accelerating nor curving, this Fin's Lift force balances, in opposite direction, with the aerodynamic side force acting on the sail (refer to Figure 2.18). For all the sailing conditions studied during this project, the Lift force was calculated in ANSYS Workbench. This Lift calculation is possible by knowing the pressure distribution along both surfaces of the Fin. The Lift force is the vector sum of the pressure times the surface area around the entire Fin, in other words, is the surface integral of the pressure along the Fin's surface area, equation 6.1.

$$L = \oint \overrightarrow{P} dA \tag{6.1}$$

So, several Lift forces were calculated for each of the proposed sailing conditions (V = 10, 15, 20, 25 knots with AoA = 2°, 4°, 6°), and for each of these cases, a few iterations were done until the solution converged. An analysis can be done to conclude about the significance of this extra-work doing the Multiple Iterations FSI analysis, comparing its results with the results of a single iteration not using the developed FSI model. In Figure 6.2, for each of the AoA, the behaviour of the Lift force with the increasing velocity is presented. In these graphs, there are also represented the Lift force results obtained by a single iteration analysis (not using the FSI model), so it is also possible to compare both results and conclude about the relevance of the Multiple Iterations FSI approach for the Lift force calculation.

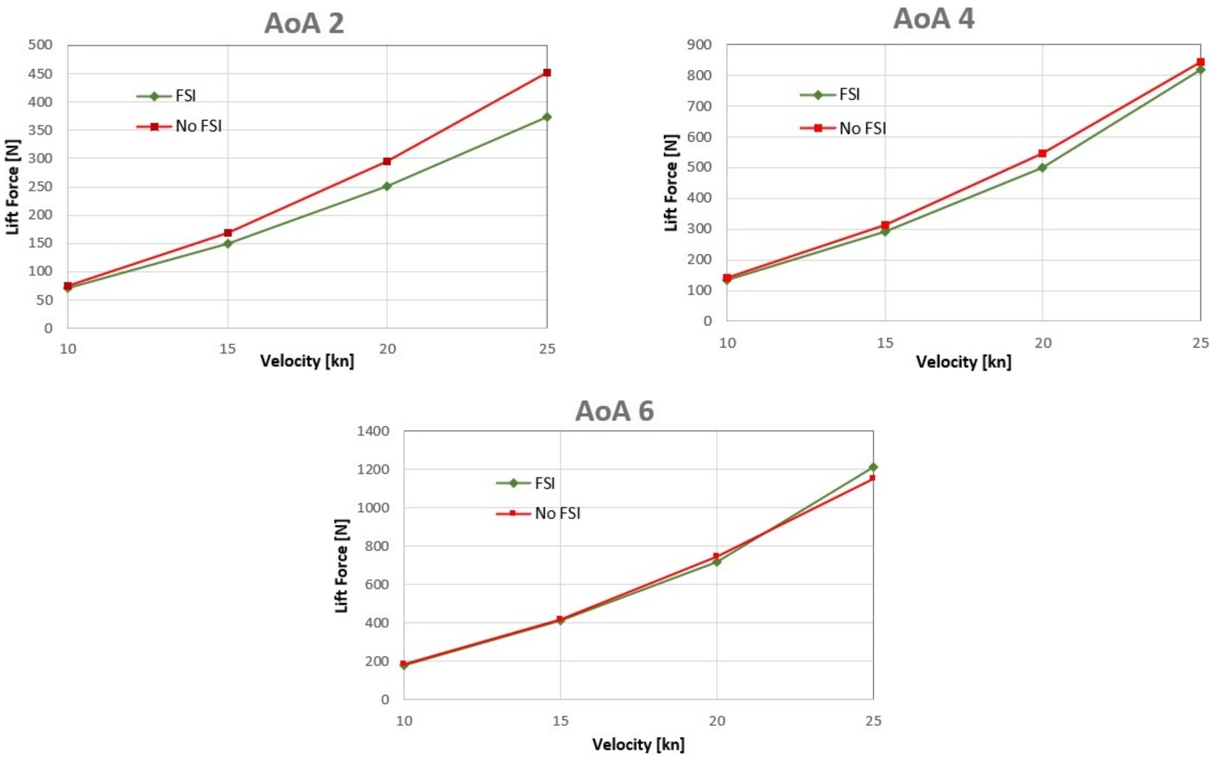

Figure 6.2: Lift Force vs. Velocity for 3 AoA with and without Multiple Iteration FSI analysis

Examining Figure 6.2, it is clear and expected the increase of the Lift force with the increasing velocity. Higher the velocity, bigger is the associated Reynolds number and higher will be the hydrodynamic forces acting on the Fin, which is what is presented in Figure 6.2.
It can be seen that the Lift follows a parabolic path with the increasing velocity. This is supported by the theory that states that the Lift force is directly proportional to the Lift coefficients and has a quadratic response to the increasing velocity. Equation 6.2 shows the Lift variation with the velocity, being L the Lift force, C_L the Lift Coefficient, ρ the fluid's density, V the fluid's velocity and A the Fin's surface area. The C_L is a constant coefficient dependent on the Fin's profile geometry.

$$L = C_L \frac{1}{2} \rho V^2 A \tag{6.2}$$

From Figure 6.2 it is also possible to compare the results with and without the Multiple Iteration FSI model. It's shown, in most of the cases, that not using FSI will result in higher Lift forces, which means that in general, simplifying these simulations by not using FSI, will create an excess in the estimation of the Fin's Lift force. This difference between using FSI and not using FSI differs for the different conditions, presenting a bigger difference for smaller angles of attack and higher velocities.
From a simple look at the graphs of Figure 6.2, it is clear that the case for which the simplification of not using FSI presents a higher difference from the "FSI" results is for an AoA of 2° and a velocity of 25 knots. This relative difference reaches 21%, so, this simplification, for this condition, will result in erroneous estimations, which supports the use of the Multiple Iteration FSI model.
As for the cases of AoA of 4° and 6°, it can be seen that both results with and without the FSI model, present similar paths being almost coincident for the AoA of 6°, where the maximum relative difference between both results reached 4.8%. These small relative differences support the simplification of a single iteration simulation (not using the FSI model) for higher angles of attack.
Not using the Multiple Iteration FSI model, will generate less accurate results, but at the same time, this simplification is significantly less time-consuming. So, a compromise between simulation time and result accuracy must be done. For the calculation of the Lift force, it can be concluded that it only makes sense to employ this simplification for AoA between 4° and 6°.
As previously said, some experimental tests to this Windsurf Fin were conducted in the Newcastle University's Emerson Cavitation Tunnel [17]. As for the measurement of hydrodynamic forces, the results obtained are good to identify a general behaviour of the Fin and the order of magnitude of the results. So, in Figure 6.3, are presented the Experimental and numerical FSI results of the Lift Coefficient vs. AoA. The necessity of analysing the Lift Coefficient is because the experimental tests were done for different conditions than the numerical simulations, namely the Reynolds number, so a dimensionless coefficient was selected to allow this comparison.

It is possible to see that the experimental tests agree with the FSI analysis result tendencies, where an increased angle of attack is accompanied by an increase of the Lift Coefficient. As previously said, these experimental results are not good for an interpretation of the absolute values, presenting a max-

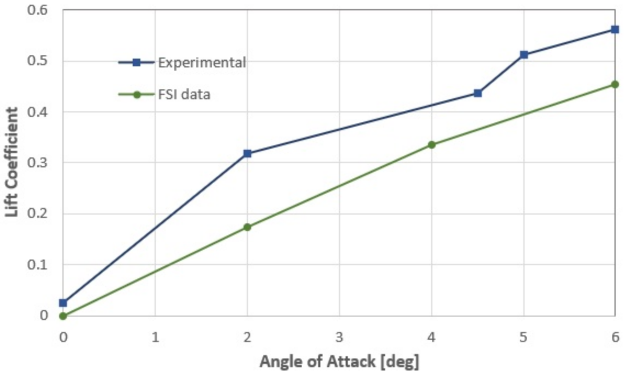

Figure 6.3: Lift Coefficient vs. AoA for the Experimental and FSI analyses

imum relative difference of 15.6% between experimental and FSI results. Also, a factor for error in this comparison is the fact that the experimental tests and the FSI simulations were not done for the same flow conditions, so the resource to the Lift Coefficient to make these two tests comparable is disregarding the possible three-dimensional effects of the Fin, increasing the possibility of eventual analysis errors.

In Appendix B.1, it can be found the results for the Lift force calculation for all the conditions studied along this project. The Lift forces presented refer to the results using the Multiple Iterations FSI model as well as the results not using this model. The relative errors for not using FSI is also presented.

6.2 Fin Deflection

The deflection is a natural behaviour of a structure simply fixed on one side and loaded along its surfaces. In the case of this Slalom Windsurf Fin, it is fixed by the base to the board and the acting pressure loads are hydrodynamically induced by the moving fluid flow. For all the simulations here done, the assumption of a static loading was assumed, disregarding possible load oscillations and the dynamic study of natural frequencies and resonance occurrence.

The Deflection analysed refers to the Fin's Tip total Deflection between the undeformed and the final deformed geometry. Figure 6.4 shows a representation on ANSYS of both the deformed and undeformed geometries of the Fin's first iteration simulation sailing at 20 knots at an AoA of 2°.

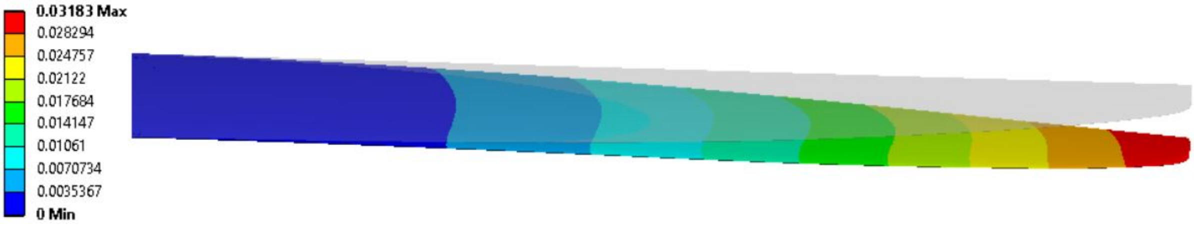

Figure 6.4: Deformed and Undeformed geometry of a Fin at 20 knots and 2° AoA (dimension in meters)

This Deflection is calculated using ANSYS structural features, simply by applying the pressure load distribution, previously calculated in the CFD analysis, to the Fin's surface and setting the fixed support boundary condition. ANSYS computes the deformation of the structure using a Finite Element Method

(FEM) analysis.

So, for each of the sailing conditions considered in this work (V = 10, 15, 20, 25 knots and AoA = 2°,4°,6°), the deflection was calculated in order to be able to conclude about the structural behaviour of the Fin when in operation. Similarly to the previous Lift analysis, here, it is also possible to conclude about the significance of this extra-work doing the Multiple Iterations FSI analysis, comparing its results with the results of a single iteration analysis not using the developed FSI model.

In Figure 6.5, it's presented the numerical results for the Fin's Tip Deflection for all the 12 different conditions. In these graphs, 2 sets of results are presented: the numerical results from the Multiple Iteration FSI model and the results from the simplification of a single iteration analysis not using the developed FSI model. The comparison between these 2 sets of data will allow for a reflection on the relevance of the Multiple Iterations FSI approach for the Tip Deflection calculation.

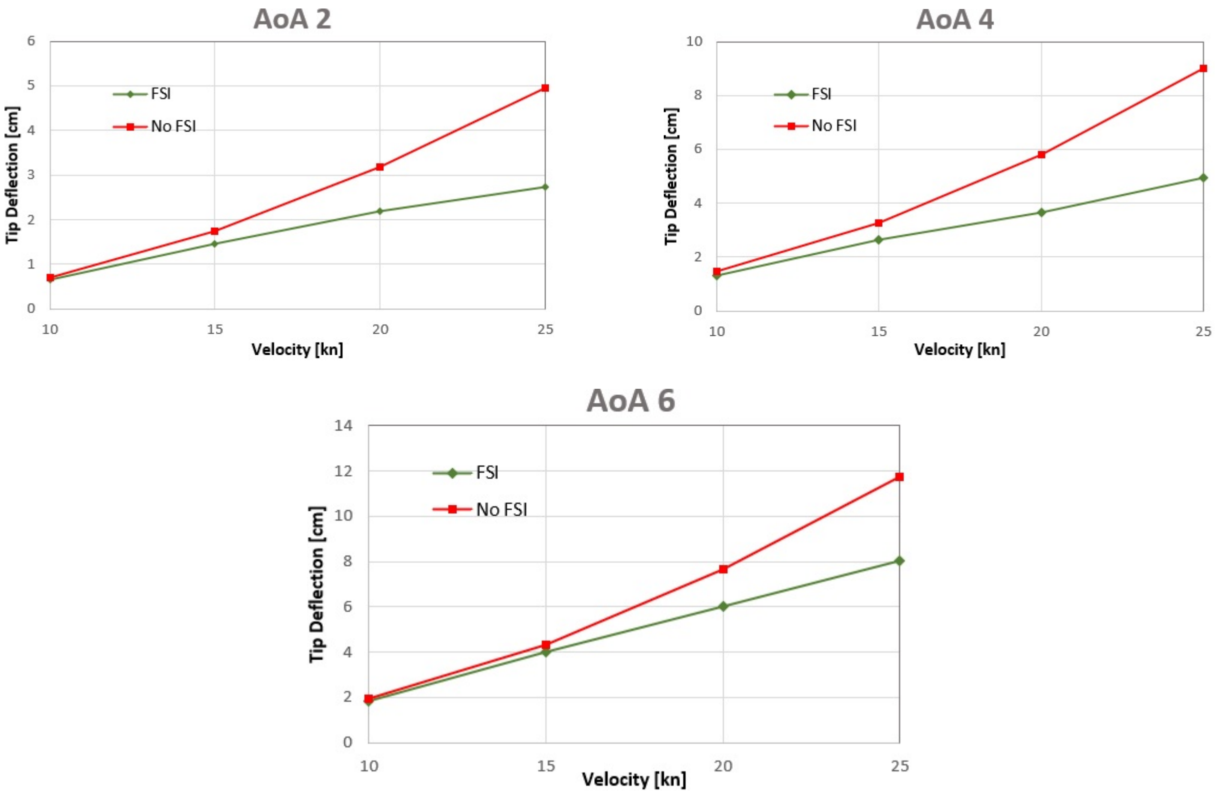

Figure 6.5: Tip Deflection vs. Velocity for 3 AoA with and without Multiple Iteration FSI analysis

Looking at Figure 6.5, a possible direct observation is related to the increase of the Deflection with the increase of velocity. Also looking at the Deflection values, it's clear that with the increasing angle of attack (until 6° before stall occurrence), the Deflection will also increase. This behaviour was already expected as the increasing velocity and increasing angle of attack are related to an increase of the hydrodynamic loads acting on the Fin which, according to Euler-Bernoulli structural beam theory [26] , provoke a higher deflection on the structure.

A comparison between the numerical results obtained by using the Multiple Iteration FSI model and using the simplification of a single iteration analysis is possible. For every condition analysed, a significant difference is clear between the ”FSI” and ”No FSI” results, being the results obtained by the single iteration simplification method (”No FSI”) always higher than the converged results (”FSI”). This means that simplifying these simulations by not using the developed FSI model, will create an excess in the estimation of the Tip Deflection.

The relative difference between ’FSI” and ”No FSI” results becomes larger for higher velocities, reaching a maximum of 82.6% for 25 knots at an AoA of 4 ° and with a minimum value of 7.6% for 15 knots at an AoA of 6°.

Another Conclusion that can be taken is the fact that this relative difference is very dependent on the velocity but not so dependent on the angle of attack, meaning that the relative error does not vary a lot with the increasing angle of attack.

As previously said in section 6.1, a compromise must be done between result accuracy and computation time, therefore a decision must be taken regarding the use of the developed FSI model or not. The fact that simplifying the simulations present such considerable errors, it can be concluded that the Multiple Iteration FSI model must be employed to give reasonable results despite the significant increase of running time.

As for a correlation between the numerical results and the experimental results obtained at Newcastle University’s Emerson Cavitation Tunnel [17], a comparison is not possible because of flawed measuring methods. The deflection was measured through photography analysis. A camera was set on the top of the water tunnel and for each flow condition, a picture was taken of the Fin’s Deformation and a following measurement was done. This method of measuring is highly susceptible to errors, and therefore this experimental data was disregarded for this analysis. Another reason why this experimental data is not considered, is because the FSI numerical simulations and the experimental tests are done for different velocity and consequently different Reynolds number, and a dimensionless parameter capable of performing a reasonable comparison between these 2 tests was not found because there is no analytic correlation between the deflection and the fluid flow velocity.

In Appendix B.2, the results for Tip Deflection are presented for all the conditions studied during this project. The Deflections presented refer to the results obtained from the Multiple Iterations FSI model as well as the results using the simplified model (No FSI). Also, the relative errors for not using FSI is presented for each of the studied cases.

6.3 Fin Twist

The Twist parameter, as the Deflection, is a natural structural behaviour of the Fin that is being pressure loaded along its surfaces. The Twist, unlike the other two parameters, is a very sensitive parameter, which means that its value fluctuates a lot with small load changes. Even though the other parameters converged, it is understandable that the Tip Twist values are still fluctuating. This is because it is possible that between ”converged” iterations, the pressure distribution is still slightly varying. This minor variation of pressure distribution along the Fin's surfaces is not significant to alter the results of Lift and total Deflection, but it is enough to change the results of a much more sensitive parameters as the Tip Twist. The fact that the dimensions of the Fin's Tip are extremely small (about 23 mm of chord and a maximum thickness of 2 mm), it makes the calculation of the Twist angle much more susceptible to small pressure distribution changes, which justifies the fact that this parameter might take longer to converge than the other two. This Twist fluctuations between "converged" iterations must have a physical explanation, such as the appearance of separation bubbles on the boundary layer and the variation of its dimensions between iterations. These recirculation bubbles interfere with the pressure distribution, the pitching momentum and consequently the structural behaviour of the Fin, so, this phenomenon might be correlated with the fluctuating values of Tip Twist.

The fact that in some cases the convergence of the Tip Twist was not achieved, it complicates the analysis of these parameters. In Figure 6.6, it's presented the Twist angle solutions for all the studied cases calculated using the Multiple Iteration FSI model.

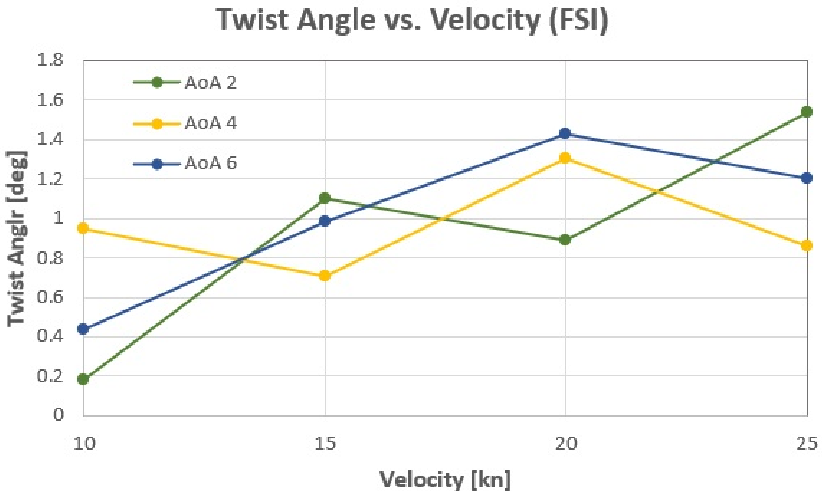

Figure 6.6: Tip Twist angle results using the Multiple Iteration FSI model

As can be seen from Figure 6.6, the results are highly inconclusive, giving only a general idea of the twisting behaviour of the Fin. From this analysis, one valuable observation that may be made is the tendency for the Twist angle to increase with the increasing velocity, and especially that the twisting of the Fin is in the direction that decreases the effective angle of attack.

As previously stated, in order to get a better understanding of the twisting behaviour, the results of the first FSI iteration can be taken into consideration. These values present a significant relative difference in relation to the "converged" solution, but it provides interesting insights on how the twist behaves with the increasing velocity and AoA, and also gives a good understanding about the Twist angles magnitude. Despite giving interesting data, these results obtained from the simplification of a single iteration FSI analysis, should not be subjected to a literal interpretation of the absolute values. In Figure 6.7, the results obtained from the first FSI iteration are presented for each of the conditions considered.

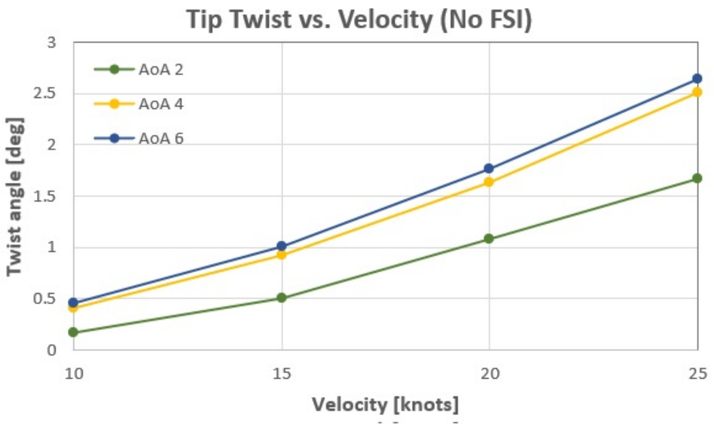

Figure 6.7: Tip Twist angle results using the simplification of a single iteration analysis

From the analysis of Figure 6.7, it can be seen that the Tip Twist angle increases with the increasing velocity, as already concluded from the analysis of Figure 6.6. Another possible observation from Figure 6.7 is the fact that the Twist values for the AoA of 4° and 6° present a very small difference between each other. To better observe this behaviour, Figure 6.8 shows the variation of the Twist angle versus the increasing angle of attack for the 4 different velocities considered. In Figure 6.8, it's presented the values at the Fin Tip and at a section at 25 cm from the Fin's Base. Also, it was established a zero-twist for the 0° AoA.

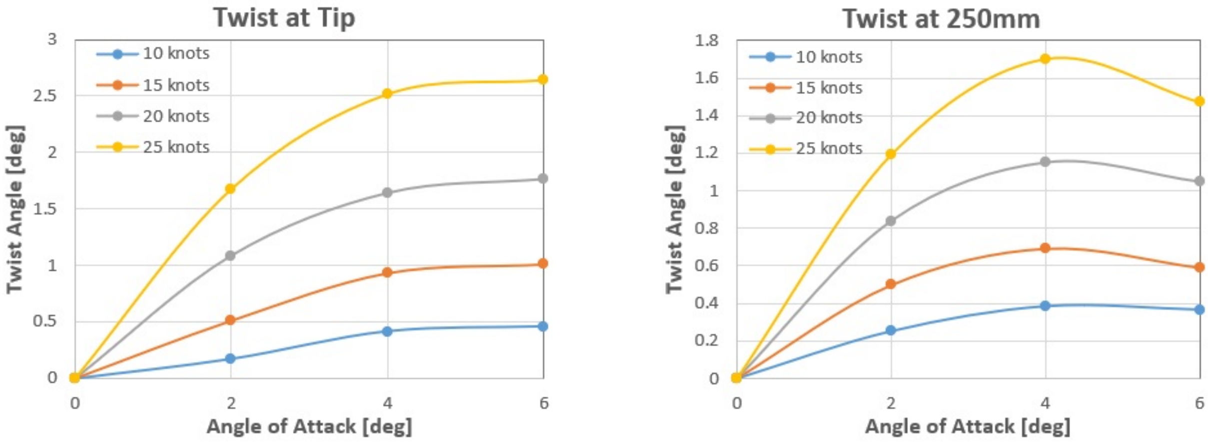

Figure 6.8: Tip Twist vs. AoA at 2 sections for 4 velocities (Not using the developed FSI model)

From Figure 6.8, it's clear the similar behaviour of the Tip Twist between both sections evaluated. For AoA higher than 4° / 6°, the twist stops increasing at the Tip and for sections nearer the Base, it starts decreasing. Also, evaluating the values of the Twist angle, it can be noted that twist angles are significantly higher at the tip. This is an expected result since the Tip is further away from the fixed support and its profile presents a much lower maximum thickness.

This behaviour of the Fin's Twist is natural and already expected. The Twist at an aerofoil shaped structure might come from two main effects: the pitching moment of the Fin's profile and the anisotropic behaviour of the structure's materials. Here the pitching moment is the moment acting on the aerodynamic centre of the aerofoil in its perpendicular direction.

The anisotropic nature of the Fin composite materials means that there is the possibility of interaction between longitudinal deflection and tip twist. In this case, it appears that the Fin lay up leads to an interaction where the effective AoA is reduced at higher AoA and velocities. This supports the theory of the Twist angle correlation with the structural composition of the Fin.

The pitching moment of the Fin's profile, when associated to the windsurf Fin, it can be interpreted as a yawing moment once the lift produced is in the horizontal direction, however, the "pitching" term will continue to be used to describe the moment acting on the Fin, perpendicular to its section and in the direction that decreases the effective AoA ("nose-down" direction in aviation terms).

The aerofoil here studied is a symmetric one and as such, it has the pressure centre (the point at which the aerodynamic forces are applied) and aerodynamic centre (the point where the pitching moment is independent of the AoA) coincident at about 1/4 of the chord behind the leading edge. Also, for symmetric aerofoils, the pressure centre doesn't change with the changing AoA. So, being the aerodynamic and pressure centre coincident for every angle of attack, it can be said that the pitching moment is zero for every condition. The zero-pitching moment happens for the symmetric aerofoil and for an infinite with constant chord and stiff wing. The fact that the symmetric Fin studied is not an infinite nor completely stiff structure and presents a non-constant chord, allows for the appearance of a non-zero pitching moment. The deflection of the Fin will make the Fin's section parallel to the incoming flow not symmetric, invalidating the assumption of coincident aerodynamic and pressure centres, and so, a pitching moment will appear. Also, the 3D effects at the Fin's tip will generate a complex pressure distribution on this region, responsible for the appearance of a complex and difficult to calculate pitching moment. In Figure 6.9, the correlation between the twisting of the Fin and the pitching moment is presented.

It's clear the similarity of behaviour of these two parameters with the increasing velocity. When the pitching moment increases, it will provoke an increase of the twisting angle. As such, it can be concluded that the pitching moment acting on the Fin contributes for the appearance of this twisting angle, together with the bend-twist coupling effect created by the composite laminate lay-up scheme. This increase of twist angle is in the direction which decreases the effective AoA, and it happens when the Fin is being overloaded and a decrease of the hydrodynamic forces is desirable.

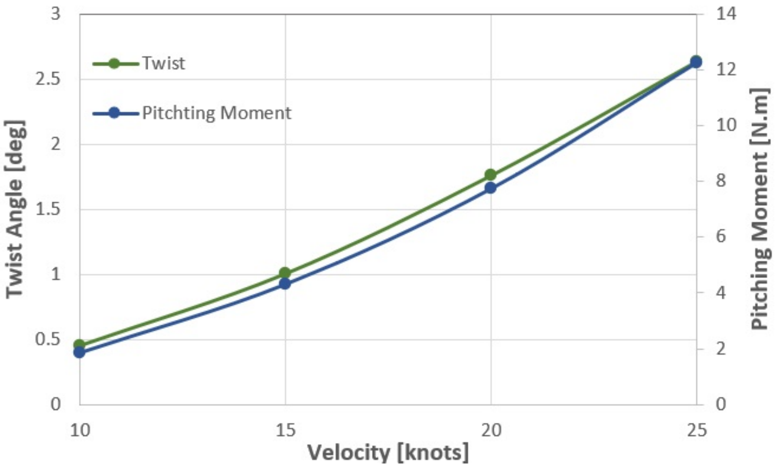

Figure 6.9: Twist Angle and Pitching Moment evolution with velocity (6° AoA)

A practical approach can be made to explain the Fin's Twist. The Twist, in the case of the studied Fin, decreases the effective angle of attack and therefore decreases the effective Lift force acting on the Fin. This decrease of Lift force is, most of the times, desirable, because this happens when the Fin is over-loaded, and a decrease of hydrodynamic loads is necessary. So, the Twist comes to solve the over-loading problem of the Fin. An analogy can be made with the sail of a boat or windsurf. The Tip of the Sail twists, decreasing the effective AoA, which decreased the aerodynamic loads. The Tip of the sail ”opens” to ”flush” the air to make this a passive region decreasing its contributing to the overall aerodynamic forces. This is desirable when the sail is being overloaded and an increase of the Lift force could be harmful. In Figure 6.10, a picture of sails can be seen where it's clear the twisting from the Base until the Tip of the sail.

Figure 6.10: Sail twist in a sailing boat (left) and windsurf (right)

Tip Twist Fluctuations:

Regarding the fluctuations of the Twisting angle, as previously said, from observation of experimental tests, the Fin's behaviour is not exactly static, presenting small structural oscillations when in operation. These oscillations are very small though, justifying the simplification of the static analysis approach done to evaluate the Fin's behaviour. The effects of these fluctuations are present on the numerical FSI analysis, mostly affecting the Fin's Twist angle, the most sensitive parameter. As previously stated, these Twist angles fluctuations should have a physical explanation that could involve the appearance of Laminar Separation Bubbles (LSB) in the vicinity of the Leading Edge.

The dimension of the Laminar Separation Bubbles (LSB) are known to have some influence on the pressure distribution of the hydrodynamic loads over the Fin and consequently interferes with the Lift, Drag and Moment acting on it. Figure 6.11 presents the pressure distribution over the suction side of an aerofoil, showing the distribution of a fully laminar flow without a LSB and of a flow with a developed LSB.

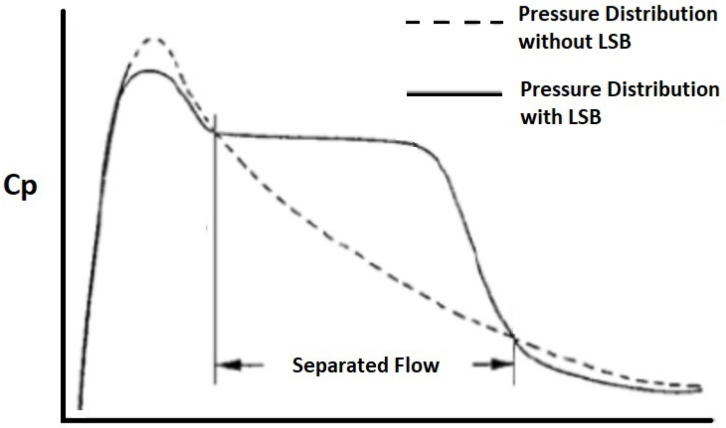

Figure 6.11: Pressure Distribution over the wing's suction side of a flow with and without a LSB

It is clear the difference between both distributions. The flow without the LSB has a pressure suction peak near the Leading Edge followed by a smooth decrease of pressure towards the Trailing Edge. The flow with the LSB, presents a smaller suction peak which is followed by a pressure plateau of constant pressure until the reattachment of a now turbulent flow, being followed by a decrease of pressure until the trailing edge. As the Lift force is the integration of this pressure distribution along the wing's surface, the variation of this pressure distribution will have some influence on this aerodynamic parameter.
From the analysis of Figure 6.11, it can be speculated the behaviour of the acting point of the Lift force with the appearance of the LSB. With the pressure distribution elongation in the direction of the trailing edge, it's foreseen a shift of the overall Lift to the aft, towards the trailing edge, moving the pressure centre in this direction. The shift of the pressure centre towards the trailing edge will increase the already existing pitching moment in the direction of reducing the effective angle of attack which is the direction of the increasing twisting angle. So, it can be expected that with the increase of the LSB length, there will be a shift of the Lift force to the aft, an increase of pitching moment and consequently an increase of the twisting angle.
To clarify these correlations, a study of the LSB's dimensions and the twisting angles can be done for every iteration of relevant FSI analyses, with the main objective to justify the fluctuations of the twisting angle. For this correlation analysis, two sailing conditions were selected: 6° AoA and a velocity of 25 and 20 knots. Due to time limitations, only the 6° AoA was studied because it is the situation that presents a bigger LSB. For smaller AoA, the LSB length are lower than 2% of the chord and so, it would have a small impact on the variations of the twisting angles in contrast with the size of LSB for 6° AoA that measures around 10% of the chord, having more effect on the Twist angle fluctuations.
A way to identify and to calculate the size of the LSB is by using Star CCM+ and the wall shear stress parameter. After the representation of the wall shear stress isolines, the reattachment point can easily be identified as the line of constant wall shear stress parallel to the leading edge. In Figure 6.12, the wall shear stress isolines are presented, where the isoline parallel to the leading edge is the region where the turbulent flow reattaches to the Fin's surface. In figure 6.13 it's shown the LSB reattaching in the region of the wall shear stress isoline.

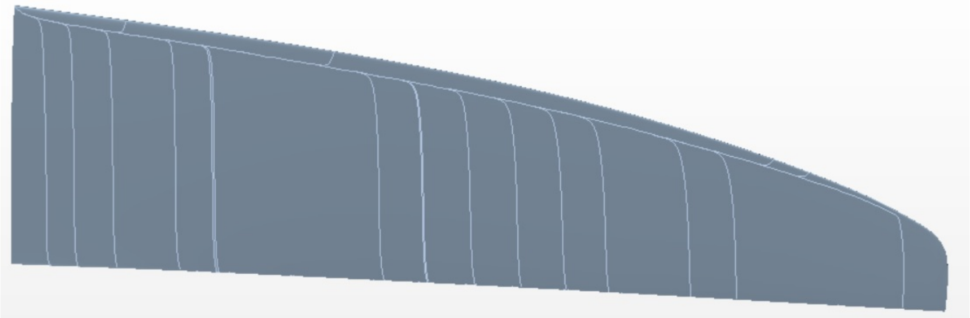

Figure 6.12: Wall Shear Stress isolines along the Fin’s surface

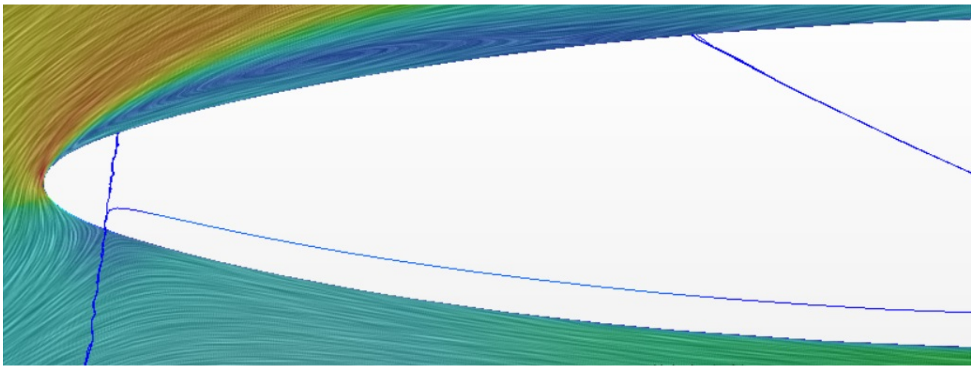

Figure 6.13: Laminar Separation Bubble at the Fin’s middle section (25 knots velocity 6° AoA)

It was selected a section at 20 cm from the Fin’s Base to monitor the variation of the LSB size along the various iterations. Figure 6.14 shows a monitor plot of the Twist angle and the size of the LSB (measured at the Fin’s middle section and relatively to the chord length) over the various iterations. Figure 6.14 presents the results for the two sailing conditions of 6° AoA and a velocity of 25 and 20 knots.

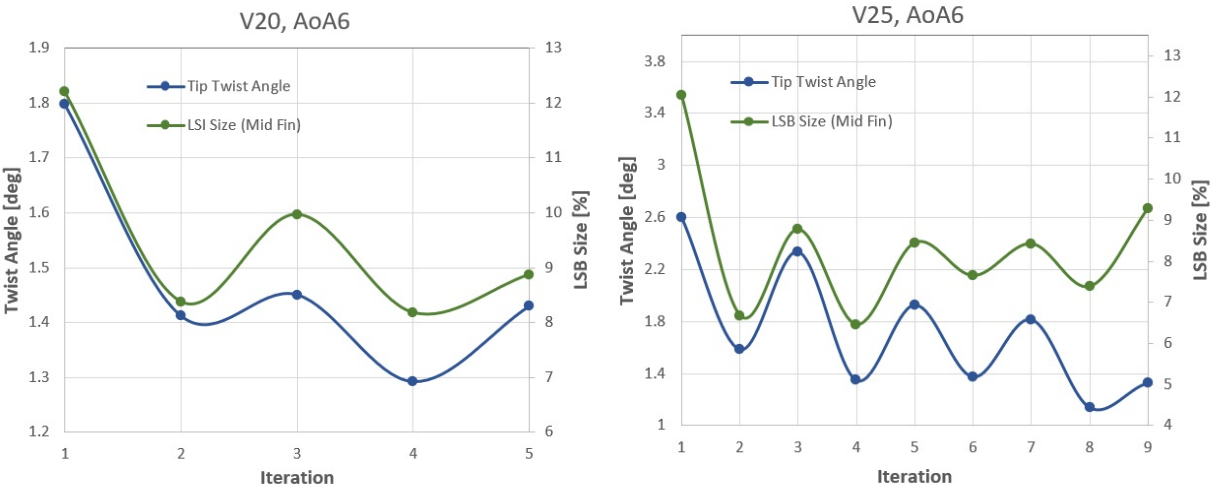

Figure 6.14: Monitor plots of Tip Twist and LSB size for two sailing conditions

The hypothesis earlier presented is in agreement with the observation of Figure 6.14. It can be observed that the behaviour of the Twist angle follows the same trend as the size of the LSB. With the increase of the LSB size, the twisting angle also accompanies this increase and vice versa, and this happens for the two cases here presented. So, it can be concluded that these oscillatory variations of LSB size between iterations are in some way responsible for the Twist fluctuations observed during the Multiple Iteration FSI analyses. Other factors could also be here involved in these fluctuations, such as the structural characteristics of the composite material plies and its anisotropic behaviour.

It is important to know that these observations are only related to the 6° AoA condition and an extrapolation of these results for different AoA could result in erroneous assumptions. Simulations with different AoA have different pressure distributions and so, the appearance of a LSB and the variation of its dimensions will have different effects on the hydrodynamic parameters [27] and consequently different effects on structural behaviours of the Fin.

A conclusion that can be made regarding the Twist angle fluctuations for 6° AoA, is that these fluctuations are linked to the oscillatory variation of the LSB size. As for lower AoA, twist fluctuations are rarely observed, but for the cases presenting these fluctuations, this correlation is not verified due to very small, and often inexistent, Laminar Separation Bubbles. For these cases, the twist fluctuation explanation should lie on the structural composition of the Fin as well as in small dynamic effects caused by the moving fluid flow around the Fin.

In Appendix B.3, it is presented the twist values for the analysis using the Multiple Iteration FSI model and the values using the simplification of a single iteration analysis (without the developed FSI model). It is also shown the different values of Twist angles and LSB size for the iterations of the two cases previously analysed (6° AoA at 20 and 25 knots of velocity).

Chapter 7

Conclusions

The principal objective of this thesis was to develop a Multiple Iteration Fluid-Structure Interaction Model, and with that, be able to make a more accurate hydrodynamic analysis of the F-Hot Slalom Windsurf Fin as well as a study of its structural behaviour when in operation.

This work follows the line of previous studies focused on this specific Fin. Before these studies, the understanding and know-how on the hydrodynamics and structural behaviour of a Fin was very limited and, with this thesis, a much wider understanding of the Fin's behaviour as well as some converged numerical values of its behaviour are obtained. The FSI process to study the behaviour of structures aero-hydrodynamically loaded is a very common and important step in the development of modern structures. The biggest challenge faced along this work was the inexistence of published documents regarding the FSI process of wing-shaped structures like the Fin here studied. So, FSI model process was developed from scratch based on the concepts spread over different scientific papers. This project was divided into different tasks:

The first step was to select the major parameters for the Hydrodynamic model, and for that, multiple verification and validation processes were conducted in order to chose proper turbulence model, transition model, physical model and to define the most significant parameters for the discretization of the computational domain. The second step was to update the Structural model making some adaptations for it to fit in the FSI model, namely the implementation of the blocks responsible for the calculation of the Δ load to be applied in each iteration. The third step was to develop the FSI process itself, which includes various iterations of the coupling between the Hydrodynamic and Structural models. These various iterations were done because converged results are wanted to give a reliability emphasis to the obtained results. The fourth and last step, was to run the developed FSI model for the 12 sailing conditions considered in order to obtain a better understanding of the structural behaviour of the Fin when in sailing mode. For the characterization of the Fin's behaviour, 3 parameters were selected: The Fin's Lift, Deflection and Twist.

7.1 Achievements

The biggest and most important achievements during this project were the selection of the major parameters to do the hydrodynamic study, the update of the already existing structural analysis process and the development of a process capable of coupling these two models into a Fluid-Structure Interaction model. The FSI model here created is a Multiple Iteration FSI model, which means that several iterations were done for each FSI analysis until a converged solution was arrived at.

As for the Structural behaviour of the Fin, it was possible a general understanding of its performance as well as the calculation of concrete values for its behaviour. The Fin's Lift force was a parameter that easily converged and a correlation between this parameter and the sailing conditions was possible. The Fin's Tip Deflection is a structural behaviour of the Fin and was also a parameter that converged allowing for a good understanding of this parameter's behaviour for the different sailing conditions. Regarding the Fin's Twist, unlike the other two parameters, for higher velocities, a convergence was difficult to achieve, mostly due to small variations of the pressure distribution on this region between iterations, creating Tip fluctuations affecting the convergence of this parameter. To understand the Twist behaviour for the different sailing conditions, a simplification of a single iteration FSI analysis was done to calculate these values, creating clear data defining the twist behaviour of the Fin, but providing results that should not be directly interpreted as absolute values of the Twist angle. Also, a possible explanation for the Twist fluctuations was provided for 6° AoA, being related to the appearance of Laminar Separation Bubbles (LSB) and their oscillatory variation of dimension.

7.2 Future Work

The work done during this thesis contributes as one of the final steps of a continuous work toward the development of a precision study of a Slalom Windsurf Fin with the objective of creating the technology capable of constructing a Fin that behaves exactly as desired. Ultimately creating a Passive Adaptive Composite (PAC), tailoring the response of the structure by changing the orientation of the composite plies. To achieve this, some work must be done to proceed with the work of the Thesis.

To facilitated the Multiple Iteration FSI analysis, it could be important to automatize this process, but for that, it would be required more resources such as a new ANSYS license that would allow a better discretization of the structural domain and consequently would allow a direct transfers of deformed geometries between the Structural and CFD models, making this a much more time-efficient process.

Also, another interesting subject would be the study of the hydrodynamic loads and distribution to understand the physics of the dynamic fluctuations at the Fin's Tip and propose some alterations to the Fin to mitigate these fluctuations.

Finally, to culminate the study of the F-Hot Slalom Windsurf Fin, it would be important to gather relevant information regarding the desired performance of the Fin and the effects that the windsurfers want to get from the use of this Fin and perform a detailed parametric study of the composite laminate scheme and ply orientation to match these requirements.

References

[1] W. Sailing. INTERNATIONAL RS:X CLASS ASSOCIATION, 2019. URL `https://www.sailing.org/classesandequipment/RSX.php`.

[2] *Impact of Composite Layup on Hydrodynamic Performance of a Surface Piercing Hydrofoil*, volume 23, Annapolis,Maryland, March 2019. Chesapeake Sailing Yacht Symposium.

[3] A. M. New York Yacht Club. 36 america's cup american magic, 2019. URL `https://americanmagic.americascup.com/`.

[4] F. hot Mouldings. F-HOT RWS SLALOM FINS, 2019. URL `http://www.f-hot.com/fins`.

[5] L. S. Sutherland. Windsurfer fin hydrodynamics. Master's thesis, University of Southampton, 1993.

[6] F. de Albuquerque Marcão Ramos do Nascimento. Windsurf fin - numerical and experimental analysis of ultimate strength. Master's thesis, Instituto Superior Técnico, 2017.

[7] E. Balzer. Development of a design tool for investigating lay-up schedule designs of a composite windsurfer fins. Master's thesis, Instituto Superior Técnico, 2018.

[8] A. M. R. dos Santos. Hydrodynamic analysis of a slalom fin of windsurf board. Master's thesis, Instituto Superior Técnico, 2018.

[9] V. de Brederode. *Fundamentos de Aerodinâmica Imcompressível*, chapter 10.2, page 559. Biblioteca do IST year = 1997.

[10] D. S. Finnicum and T. J. Hanratty. Effect of favorable pressure gradients on turbulent boundary layers. *AIChE Journal*, 34(4):529–540, April 1998.

[11] U. Goldberg, O. Peroomian, S. Palaniswamy, and S. Chakravarthy. Anisotropic k-epsilon model for adverse pressure gradient flow. *AIAA Journal*, January 1999.

[12] F. R. Menter. Zonal two equation $k-\omega$ turbulence models for aerodynamic flows. *AIAA Journal*, 1993.

[13] F. R. Menter. Two-equation eddy-viscosity turbulence models for engineering applications. *AIAA Journal*, 32(8):1598–1605, 1994.

[14] F. R. Menter. Correlation-based transition modeling for unstructured parallelized computational fluid dynamics codes. *AIAA Journal*, 47(12), 2009.

[15] P. Malan. Calibrating the $\gamma - re_\theta$ transition model for commercial cfd. In *47th AIAA Aerospace Sciences Meeting*, January 2009.

[16] L. S. Sutherland. A review of impact testing on marine composite materials: Part i â marine impacts on marine composites. *Composite Structures*, 188:197–208, March 2018.

[17] K. Tansley. Investigation into windsurf fin hydridynamics - a practical study. Master's thesis, Newcastle University, 2018.

[18] M. H. Sharqawy, J. H. Lienhard, and S. M. Zubair. Thermophysical properties of seawater: A review and new correlations that include pressure dependence. *Desalination and Water Treatment*, 16:354–380, 2010.

[19] H. M. Drela. Xfoil 6.94 user guide, 2001.

[20] SIEMENS. User guide star-ccm+ version 7.02.008. *CD-adapco*, 2011.

[21] P. J. Roache. *Verification and Validation in Computational Science and Engineering*. Albuquerque, New Mexico: Hermosa Publishers, 1998.

[22] R. E. Sheldahl and P. C. Klimas. *Aerodynamic Characteristics of Seven Symmetrical Airfoil Sections Through 180-Degree Angle of Attack for Use in Aerodynamic Analysis of Vertical Axis Wind Turbines*. Sandia National Laboratories, 1981. United Stated Department of Energy.

[23] A. Firooz and M. Gadami. *Turbulence flow for naca 4412 in unbounded fow and ground effect*. International Conference on Boundary and Interior Layers, 2006.

[24] L. Eça and M. Hoekstra. The numerical friction line. J Mar Sci Technol, 13:328-345. 2008.

[25] N. Sørensen. Cfd modelling of laminar-turbulent transition for airfoils and rotors using the gamma-re-theta model. Technical Report 12:715-733, Wind Energy, 2009.

[26] F. P. Beer and E. R. Johnston. *Mecânica dos Materiais*, chapter 5, pages 327–390. McGraw Hill, 5 edition, 2011.

[27] P. L. Delafin, F. Deniset, and J.-A. Astolfi. Effect of the laminar separation bubble induced transition on the hydrodynamic performance of a hydrofoil. *European Journal of Mechanics*, 46:190–200, Nov 2014.

Appendix A

Turbulence Models Governing Equations

A.1 Standard $k - \epsilon$ Turbulence Model

Equation for Turbulent Kinetic Energy (k):

$$u\frac{\partial k}{\partial x} + v\frac{\partial k}{\partial y} = \nu_t S^2 + \nabla . \left(\left(\nu + \frac{\nu_t}{\sigma_k} \right) \nabla k \right) - \epsilon \tag{A.1}$$

Equation for dissipation of Turbulent kinetic energy (ϵ):

$$u\frac{\partial \epsilon}{\partial x} + v\frac{\partial \epsilon}{\partial y} = C_1 \frac{\epsilon}{k} \nu_t S^2 + \nabla \left(\left(\nu + \frac{\nu_t}{\sigma_\epsilon} \right) \nabla \epsilon \right) - C_2 \frac{\epsilon^2}{k} \tag{A.2}$$

Turbulent viscosity (ν_t) is modelled as:

$$\mu_t = C_\mu \frac{k^2}{\epsilon} \tag{A.3}$$

The Model Constants are:

$$C_1 = 1.44 \quad , \quad C_2 = 1.92 \quad , \quad C_\mu = 0.09 \quad , \quad \sigma_k = 1.0 \quad , \quad \sigma_\epsilon = 1.3 \tag{A.4}$$

A.2 SST $k-\omega$ Turbulence Model

Equation for Turbulent Kinetic Energy (k):

$$\frac{\partial k}{\partial t}+U_j\frac{\partial k}{\partial x_j}=P_k-\beta^* k\omega+\frac{\partial}{\partial x_j}\left[(\nu+\sigma_k\nu_T)\frac{\partial k}{\partial x_j}\right] \tag{A.5}$$

Equation for Specific Dissipation Rate (ω):

$$\frac{\partial \omega}{\partial t}+U_j\frac{\partial \omega}{\partial x_j}=\alpha S^2-\beta\omega^2+\frac{\partial}{\partial x_j}\left[(\nu+\sigma_\omega\nu_T)\frac{\partial \omega}{\partial x_j}\right]+2(1-F_1)\sigma_{\omega^2}\frac{1}{\omega}\frac{\partial k}{\partial x_i}\frac{\partial \omega}{\partial x_i} \tag{A.6}$$

The Kinematic Eddy Viscosity is given by:

$$\nu_T=\frac{a_1 k}{max(a_1\omega, SF_2)} \tag{A.7}$$

Auxiliary Relations:

$$F_2=tanh\left[\left[max\left(\frac{2\sqrt{k}}{\beta^*\omega y},\frac{500\nu}{y^2\omega}\right)\right]^2\right] \tag{A.8}$$

$$P_k=min\left(\tau_{ij}\frac{\partial U_i}{\partial x_j},10\beta^* k\omega\right) \tag{A.9}$$

$$F_1=tanh\left\{\left\{min\left[max\left(\frac{\sqrt{k}}{\beta^*\omega y},\frac{500\nu}{y^2\omega}\right),\frac{4\sigma_{\omega^2}k}{CD_{k\omega}y^2}\right]\right\}^4\right\} \tag{A.10}$$

$$CD_{k\omega}=max\left(2\rho\sigma_{\omega^2}\frac{1}{\omega}\frac{\partial k}{\partial x_i}\frac{\partial \omega}{\partial x_i},10^{-10}\right) \tag{A.11}$$

The Closed Coefficients are the following:

(α and β are calculated using the formula $\phi=\phi_1F_1+\phi_2(1-F_1)$)

$$\alpha_1=\frac{5}{9} \quad , \quad \alpha_2=0.44 \tag{A.12}$$

$$\beta_1=\frac{3}{40} \quad , \quad \beta_2=0.0828 \tag{A.13}$$

$$\beta^*=\frac{9}{100} \tag{A.14}$$

$$\sigma_{k1}=0.85 \quad , \quad \sigma_{k2}=1 \quad , \quad \sigma_{\omega 1}=0.5 \quad , \quad \sigma_{\omega 2}=0.856 \tag{A.15}$$

A.3 Spalart-Allmaras Turbulence Model

The Spalart-Allmaras turbulent model is a one-equation model solving for $\widetilde{\nu}$ and is given by:

$$\frac{\partial \widetilde{\nu}}{\partial t} + u_j \frac{\partial \widetilde{\nu}}{\partial x_j} = C_{b1}[1 + f_{t2}]\widetilde{S}\widetilde{\nu} + \frac{1}{\sigma}\left\{\nabla.[(\nu + \widetilde{\nu})\nabla\widetilde{\nu}] + C_{b2}|\nabla\widetilde{\nu}|^2\right\} - \left[C_{\omega 1} f_\omega - \frac{C_{b1}}{k^2} f_{t2}\right]\left(\frac{\widetilde{\nu}}{d}\right)^2 + f_{t1}\Delta U^2 \tag{A.16}$$

The Turbulent Eddy Viscosity is a function o $\widetilde{\nu}$ and is given by:

$$\nu_t = \widetilde{\nu} f_{v1} \quad , \quad f_{v1} = \frac{\chi^3}{\chi^3 + C_{v1}^3} \quad , \quad \chi := \frac{\widetilde{\nu}}{\nu} \tag{A.17}$$

Other correlations are given by:

$$\widetilde{S} \equiv S + \frac{\widetilde{\nu}}{k^2 d^2} f_{v2} \quad , \quad f_{v2} = 1 - \frac{\chi}{1 + \chi f_{v1}} \tag{A.18}$$

$$f_\omega = g\left[\frac{1 + C_{\omega 3}^6}{g^6 C_{\omega 3}^6}\right]^{\frac{1}{6}} \quad , \quad g = r + C_{\omega 2}(r^6 - r) \quad , \quad r \equiv \frac{\widetilde{\nu}}{\widetilde{S} k^2 d^2} \tag{A.19}$$

$$f_{t1} = C_{t1} g_t exp\left(-C_{t2}\frac{\omega_t^2}{\Delta U^2}[d^2 + g_t^2 d_t^2]\right) \quad , \quad f_{t2} = C_{t3} exp(-C_{tA}\chi^2) \tag{A.20}$$

$$S = \sqrt{2\Omega_{ij}\Omega_{ij}} \quad , \quad \Omega_{ij} = \frac{1}{2}\left(\frac{\partial u_i}{\partial x_j} - \frac{\partial u_j}{\partial x_i}\right) \tag{A.21}$$

The model constants are:

$$\sigma = \frac{2}{3} \quad , \quad C_{b1} = 0.1355 \quad , \quad C_{b2} = 0.622 \quad , \quad k = 0.41 \quad , \quad C_{\omega 1} = \frac{C_{b1}}{k^2} + \frac{1 + C_{b2}}{\sigma} \tag{A.22}$$

$$C_{\omega 2} = 0.3, \quad C_{\omega 3} = 2 \quad , \quad C_{v1} = 7.1 \quad , \quad C_{t1} = 1 \quad , \quad C_{t2} = 2 \quad , \quad C_{t3} = 1.2 \quad , \quad C_{t4} = 0.5 \tag{A.23}$$

Appendix B

Numerical Results

B.1 Lift Force

The Lift force was calculated for 12 different sailing conditions: 3 angles of attack and 4 velocities. The next tables show the numerical results obtained by the simulation of the Slalom Windsurf Fin tested for all these conditions. Two different Lift values are presented for each condition: the value obtained using the Multiple Iterations FSI model developed in this thesis, and the value obtained by using the simplification of a single iteration analysis not using the developed FSI model. For reference purposes, it is also presented the relative difference between both results.

Velocity [knots]	Lift (FSI) [N]	Lift (No FSI) [N]	Relative Difference [%]
10	70.81	74.71	5.49
15	149.79	168.44	12.45
20	250.61	294.49	17.51
25	372.69	452.78	21.49

Table B.1: Lift Force Numerical Results for an AoA 2°

Velocity [knots]	Lift (FSI) [N]	Lift (No FSI) [N]	Relative Difference [%]
10	135.44	140.02	3.38
15	293.40	311.86	6.29
20	500.86	545.78	8.97
25	818.35	842.24	2.92

Table B.2: Lift Force Numerical Results for an AoA 4°

Velocity [knots]	Lift (FSI) [N]	Lift (No FSI) [N]	Relative Difference [%]
10	182.65	188.35	3.12
15	412.29	421.15	2.15
20	718.07	747.52	4.10
25	1210.70	1152.13	4.84

Table B.3: Lift Force Numerical Results for an AoA 6°

B.2 Tip Deflection

Similarly to the previous case of Lift force calculation, the following tables present the Tip Deflection results for the 12 different sailing conditions considered along this work. The results from the Multiple Iterations FSI analysis as well as the results from the simplified approach of not using the developed FSI model are presented. For reference purposes, it is also shown the relative difference between both results.

Velocity [knots]	Deflection (FSI) [cm]	Deflection (No FSI) [cm]	Relative Difference [%]
10	0.660331	0.71472	8.236667
15	1.463989	1.7463	19.2837
20	2.180599	3.183	45.96908
25	2.722041	4.9631	82.33012

Table B.4: Tip Deflection Numerical Results for an AoA 2°

Velocity [knots]	Deflection (FSI) [cm]	Deflection (No FSI) [cm]	Relative Difference [%]
10	1.329114	1.4616	9.968032
15	2.649013	3.283	23.93296
20	3.651591	5.8042	58.94989
25	4.927136	9.0011	82.68423

Table B.5: Tip Deflection Numerical Results for an AoA 4°

Velocity [knots]	Deflection (FSI) [cm]	Deflection (No FSI) [cm]	Relative Difference [%]
10	1.812342	1.955	7.871495
15	4.01145	4.3174	7.626929
20	6.042869	7.674	26.99266
25	8.051302	11.764	46.11302

Table B.6: Tip Deflection Numerical Results for an AoA 6°

B.3 Tip Twist

The following tables present the values of the Twist angle at the Tip of the Fin using the Multiple Iteration FSI model and also the results using the simplification of a single iteration FSI analysis.

Velocity [knots]	Twist (FSI) [deg]	Twist (No FSI) [deg]	Relative Difference [%]
10	0.179068	0.171268	4.356158
15	1.097365	0.509865	53.53731
20	0.884677	1.084868	22.62869
25	1.539176	1.673017	8.695662

Table B.7: Tip Twist Numerical Results for a 2° AoA

Velocity [knots]	Twist (FSI) [deg]	Twist (No FSI) [deg]	Relative Difference [%]
10	0.943623	0.41285	56.24844
15	0.703644	0.9298	32.14059
20	1.307191	1.637796	25.29127
25	0.857049	2.511693	193.0631

Table B.8: Tip Twist Numerical Results for a 4° AoA

Velocity [knots]	Twist (FSI) [deg]	Twist (No FSI) [deg]	Relative Difference [%]
10	0.437427	0.455492	4.129937
15	0.983782	1.007466	2.407394
20	1.427814	1.76073	23.31647
25	1.201258	2.636758	119.4998

Table B.9: Tip Twist Numerical Results for a 6° AoA

From a simple look at the relative difference between the ”FSI” and ”No FSI” results, it’s clear the substantial magnitude of these values. This could be a clue not to use the values from the simplification method (”No FSI”), but after analyzing the values of the FSI results, it can be concluded that it’s these values that are inadequately calculated. As previously stated, these inadequacies of calculations are derived from the fact that the Fin when in operation presents a small oscillatory behavior at the Tip, affecting mostly the Tip Twist angle, the most sensitive parameter. So, the values of the simplified model (”No FSI”) are used to evaluate the structural behavior of the Fin.

The following tables present the Tip Twist angle and the relative length of the Laminar Separation Bubble (LSB) for each iteration of the two presented studied cases: 6° AoA and 25 and 20 knots of velocity. These values are represented in the graphs of Figure 6.14.

Velocity - 20 knots, AoA - 6°

Iteration	Twist Angle [deg]	LSB length (Mid Fin) [%]
1	1.797873	12.19778
2	1.412049	8.3786
3	1.450344	9.967473
4	1.291929	8.180944
5	1.429441	8.872102

Table B.10: Tip Twist angle and LSB size monitor using the Multiple Iteration FSI model (20 knots velocity and 6° AoA)

Velocity - 25 knots, AoA - 6°

Iteration	Twist Angle [deg]	LSB length (Mid Fin) [%]
1	2.603816	12.03679
2	1.58581	6.681725
3	2.338073	8.775937
4	1.347796	6.460112
5	1.928951	8.455237
6	1.373539	7.648721
7	1.816035	8.425536
8	1.137263	7.385748
9	1.326122	9.292076

Table B.11: Tip Twist angle and LSB size monitor using the Multiple Iteration FSI model (25 knots velocity and 6° AoA)